J. Fluid Mech. (2024), *vol*. 997, A76, doi:10.1017/jfm.2024.799

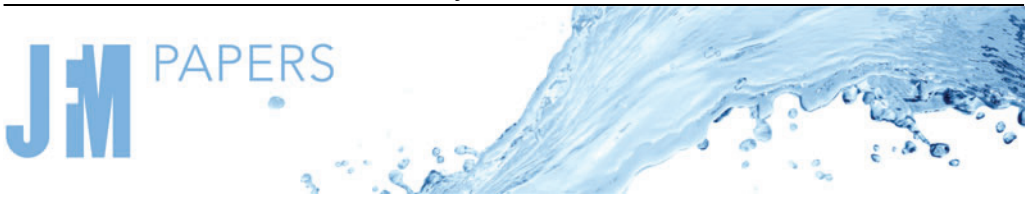

Direct numerical simulation of turbulent, generalized Couette–Poiseuille flow

Y. Zhang[1], **D.I. Pullin**[2], **W. Cheng**[1],† **and X. Luo**[1]

[1]School of Engineering Science, University of Science and Technology of China, Hefei 230026, PR China
[2]Graduate Aerospace Laboratories, California Institute of Technology, CA 91125, USA

(Received 4 December 2023; revised 29 April 2024; accepted 16 June 2024)

We present direct numerical simulation (DNS) and modelling of incompressible, turbulent, generalized Couette–Poiseuille flow. A particular example is specified by spherical coordinates (Re, θ, ϕ), where $Re = 6000$ is a global Reynolds number, ϕ denotes the angle between the moving plate, velocity-difference vector and the volume-flow vector and $\tan\theta$ specifies the ratio of the mean volume-flow speed to the plate speed. The limits $\phi \to 0^\circ$ and $\phi \to 90^\circ$ give alignment and orthogonality, respectively, while $\theta \to 0^\circ$, $\theta \to 90^\circ$ correspond respectively to pure Couette flow in the x direction and pure Poiseuille flow at angle ϕ to the x axis. Competition between the Couette-flow shear and the forced volume flow produces a mean-velocity profile with directional twist between the confining walls. Resultant mean-speed profiles relative to each wall generally show a log-like region. An empirical flow model is constructed based on component log and log-wake velocity profiles relative to the two walls. This gives predictions of four independent components of shear stress and also mean-velocity profiles as functions of (Re, θ, ϕ). The model captures DNS results including the mean-flow twist. Premultiplied energy spectra are obtained for symmetric flows with $\phi = 90^\circ$. With increasing θ, the energy peak gradually moves in the direction of increasing k_x and decreasing k_z. Rotation of the energy spectrum produced by the faster moving velocity near the wall is also observed. Rapid weakening of a spike maxima in the Couette-type flow regime indicates attenuation of large-scale roll structures, which is also shown in the Q-criterion visualization of a three-dimensional time-averaged flow.

Key words: turbulence simulation, turbulence modelling

1. Introduction

Turbulent flow between two parallel, plane walls of separation $2h$ and driven by either an applied pressure gradient or moving boundaries, provides several canonical flow configurations of interest in the study of wall-bounded turbulence. In pressure-gradient driven, turbulent plane Poiseuille (PP) flow, coherent structures tend to show similar

† Email address for correspondence: wancheng@ustc.edu.cn

features to those observed in other natural wall-bounded flows (Lee & Moser 2015), such as boundary layers (Jodai & Elsinga 2016) and pipe flows (Lee, Sung & Adrian 2019). In contrast, plane-Couette (PC) flow turbulence (Lee & Moser 2018) generated by differential top/bottom-wall motion displays the formation of coherent streamwise rolls with spanwise spacing of order several h, with strong effects on mixing enhancement. The rolls persist to large Reynolds numbers (Cheng, Pullin & Samtaney 2022).

Kim, Moin & Moser (1987) performed direct numerical simulation (DNS) of PP flow, followed by further similar studies (del Álamo & Jiménez 2003; del Álamo *et al.* 2004; Hoyas & Jiménez 2006; Lozano-Durán & Jiménez 2014). An important feature of PP flow is the existence of a log region in the wall-normal mean-velocity profile at sufficiently large Reynolds number, first predicted by von Kármán (1930) and later refined by Millikan (1938), and subsequently confirmed by both DNS and experiment, for example, Moser, Kim & Mansour (1999) at wall-friction Reynolds number $Re_\tau \approx 590$, Bernardini, Pirozzoli & Orlandi (2014) with $Re_\tau \approx 4000$ and Lee & Moser (2015) up to $Re_\tau = 5200$. Mean-velocity scaling for PC flow shows features in common with PP flow (Pirozzoli, Bernardini & Orlandi 2014), but perhaps with differences inferred from a mean momentum analysis (Wei, Fife & Klewicki 2007).

Large-scale structures found in PC flow include streamwise streaks and rollers, roll behaviour slightly above the turbulent transition state (Tillmark & Alfredsson 1998), low-Reynolds-number effects (Kitoh, Nakabyashi & Nishimura 2005) and roll extension in the streamwise direction (Lee & Moser 2018). Comparison of PP and PC flow features have focused on streamwise turbulent intensities (Ostilla-Mónico *et al.* 2016), energy spectra (Lee & Moser 2018) and the wall skin-friction coefficient, turbulent kinetic energy budget and Reynolds stress components (Orlandi, Bernardini & Pirozzoli 2015).

A combination of shear produced by relative wall movement and an externally applied pressure gradient generates so-called plane Couette–Poiseuille (PCP) flow. Competition between the two mechanisms produces new flow characteristics. An early experimental study by Telbany & Reynolds (1980) gave an empirical description of the viscous, log, gradient layers and core regions. Improvements in our understanding of PCP flow physics was provided by Thurlow & Klewicki (2000), who observed a locally negative production of streamwise turbulence near the moving wall, and Nakabayashi, Kitoh & Katoh (2004), who explored similarity laws in the mean-velocity profiles. Plane Couette–Poiseuille flow with zero mean shear stress at one wall was investigated by Coleman *et al.* (2017), Yang, Zhao & Andersson (2017) and Choi, Lee & Hwang (2021), with emphasis on an extended log region for the mean-velocity profile. Pirozzoli, Bernardini & Orlandi (2011) analysed the transition process from pure Couette to pure Poiseuille flow using conditional eddy methodology while Gandía-Barberá *et al.* (2018) investigated the relation between Reynolds stresses and roll disappearance. Direct numerical simulation and both wall-resolved and wall-modelled large-eddy simulations (LES) of PCP flow was discussed by Cheng *et al.* (2023) who also developed an empirical mean-flow model from which the critical flow parameters signalling the transition from PC-dominated to PP-dominated flow, where the mean shear stress on one wall vanishes, could be predicted as a function of an overall Reynolds number.

In general, the flow between two plane, parallel walls forced by combined uniform wall relative motion and a constant wall-parallel applied pressure gradient can be characterized in a space of three parameters consisting of two independent Reynolds numbers and an angle between the moving plates velocity-difference vector and the mean volume-flow vector. We call this generalized Couette–Poiseuille (GCP) flow. Plane Couette–Poiseuille flow is then the special case with two-vector alignment. Generalized Couette–Poiseuille

flow is worthy of study first because it provides an interesting and unusual example of a canonical wall-bounded turbulent flow that exhibits four independent skin-friction components together with a wall-parallel mean-velocity profile that will exhibit directional twist or rotation as a function of the normal distance from either wall. This flow then has parallels with some aspects of three-dimensional boundary layers. Further, its fluid-dynamical richness and relative simplicity for numerical simulation presents a useful and challenging test flow for both the Reynolds-averaged Navier–Stokes equations and also for wall-modelled LES owing to the need for two-component mean velocity and skin-friction analysis in the near-wall region. It is therefore of interest to explore the characteristics of GCP flow that include variation in both wall skin-friction vectors, the behaviour of the mean-velocity profile including the possible existence of a log-like region and the existence of large-scale flow structures in the presence of competition between the non-aligned Couette-flow shear and the externally applied pressure gradient. This is the subject of the present study.

In § 2 we define the independent flow parameters for GCP flow and describe briefly the present DNS numerical method. The misalignment between the mean volume-flow vector and the mean pressure-gradient vector is clarified. To help appreciate the three-dimensional mean-flow character, we first focus in § 3 on the special and interesting limit of orthogonality between the wall-relative-velocity and volume-flow vectors, referred to as orthogonal Couette–Poiseuille (OCP) flow. This shows some basic features of the wall skin-friction vectors and mean-flow properties. In § 4 we provide an empirical modelling framework for GCP flow based on use of log-wake profiles for component, mean-flow velocity components relative to both top and bottom walls. Comparison of mean-flow diagnostics between DNS and modelling is developed in § 5. The three-dimensional behaviour of mean-velocity profiles with emphasis on the mean-flow, twist angle distributions is also studied. In § 6 the three-dimensional geometry of the premultiplied energy spectra are studied in order to show the kinetic energy distribution at different length scales in the transition from Couette flow to Poiseuille flow, but only for the special case of OCP flow. Visualization of selected time-averaged three-dimensional flow structures is also discussed. Concluding remarks are given in § 7.

2. Flow description, numerical method and simulations performed

2.1. *Description of GCP flow*

A sketch of GCP flow is shown in figure 1 in a right-handed Cartesian coordinate frame (x, y, z) with corresponding velocity components (u, v, w). Here, x is the wall-moving direction and y is the wall-normal direction. The distance between the top wall and the bottom wall is $L_y = 2h$ while L_x and L_z are domain sizes in the (x, z) directions, respectively. The top and bottom walls move in the x direction with velocity components $(-U_c, 0, 0)$ and $(U_c, 0, 0)$, respectively. Misalignment between the pressure-gradient vector and the wall-velocity-difference vector results in volume flows in both the (x, z) directions with characteristic velocities

$$U_{Vx} = \frac{1}{2h}\int_{-h}^{h} U(y)\,\mathrm{d}y, \quad U_{Vz} = \frac{1}{2h}\int_{-h}^{h} W(y)\,\mathrm{d}y, \tag{2.1a,b}$$

with $U(y)$ and $W(y)$ volume-time-averaged mean-velocity profiles corresponding to velocity components u and w. Other useful velocities are the resultant bulk velocity $U_V = ({U_{Vx}}^2 + {U_{Vz}}^2)^{1/2}$ and the general velocity scale $U_0 = (U_c^2 + {U_{Vx}}^2 + {U_{Vz}}^2)^{1/2}$.

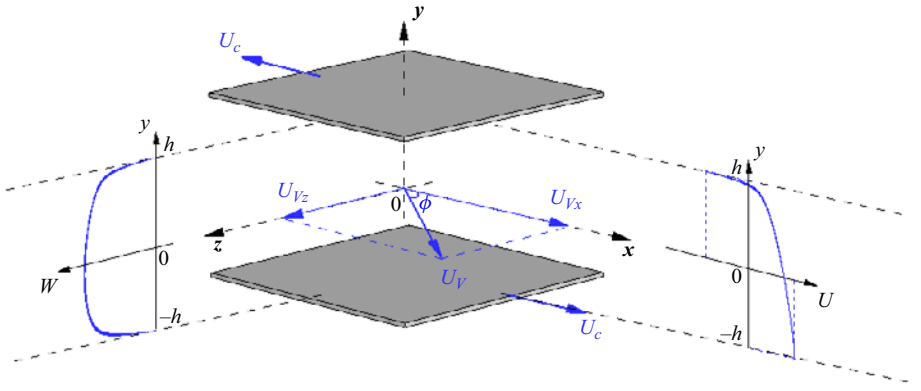

Figure 1. Sketch of generalized Couette–Poiseuille (GCP) flow. The separation distance between the top wall and the bottom wall is $L_y = 2h$, while the domain sizes in x and z are L_x and L_z, respectively. The wall-moving velocities of the top and bottom walls are $-U_c$ and U_c, as denoted by blue arrows. The angle $\phi = \arctan(Re_{Vz}/Re_{Vx})$ is the ratio of the volume flow in the x and z directions. The angle $\theta = \arctan[(Re_{Vx}^2 + Re_{Vz}^2)^{1/2}/Re_c]$. Left and right blue lines show the projection of sketched velocity profiles in the z–y plane and the x–y plane.

The three velocities ($U_c \geq 0$, $U_{Vx} \geq 0$, $U_{Vz} \geq 0$) have associated Reynolds numbers

$$Re_c = \frac{U_c h}{\nu}, \quad Re_{Vx} = \frac{U_{Vx} h}{\nu}, \quad Re_{Vz} = \frac{U_{Vz} h}{\nu}, \tag{2.2a–c}$$

with ν the kinematic viscosity of the fluid.

The parameter set ($Re_c \geq 0$, $Re_{Vx} \geq 0$, $Re_{Vz} \geq 0$) forms the all-positive octant of a Cartesian space. It will be convenient to work with spherical coordinates (Re, θ, ϕ) where

$$Re_c = Re\cos\theta, \quad Re_{Vx} = Re\sin\theta\cos\phi, \quad Re_{Vz} = Re\sin\theta\sin\phi, \tag{2.3a–c}$$

with inversion

$$Re = \frac{U_0 h}{\nu}, \quad Re_V = \frac{U_V h}{\nu}, \tag{2.4a}$$

$$\theta = \arctan\left(\frac{Re_V}{Re_c}\right), \quad \theta \in [0^\circ, 90^\circ], \tag{2.4b}$$

$$\phi = \arctan\left(\frac{Re_{Vz}}{Re_{Vx}}\right), \quad \phi \in [0^\circ, 90^\circ]. \tag{2.4c}$$

Here Re_V is a Reynolds number corresponding to the resultant bulk velocity U_V and Re is taken as the defining global Reynolds number based on the general velocity scale U_0, $\tan\theta = U_V/U_c$ can be interpreted as the relative weighting of Poiseuille-type to Couette-type flow and ϕ denotes the angle made by the bulk velocity vector $(U_{Vx}, 0, U_{Vz})$ with the plate velocity-difference vector $(2U_c, 0, 0)$.

For $\theta = 0^\circ$, $Re_{Vx} = Re_{Vz} = Re_V = 0$ and the flow reduces to PC flow in the x direction. When $\theta = 90^\circ$, $Re_c = 0$ and the flow becomes PP flow with net volume flow aligned with ϕ. When $\phi = 0^\circ$, both the plate velocity-difference vector and the volume-flow vector are aligned in the x direction, as discussed by Cheng *et al.* (2023). This is PCP flow. When $\phi = 90^\circ$, the volume-flow vector is perpendicular to the moving plates velocity-difference vector. This orthogonality results in a centrosymmetric ensemble-mean

flow with the centre of symmetry at the origin of (x, y, z) space, a property that exists only for $\phi = 90^\circ$.

Sketches of typical mean-velocity profiles in both the y–z plane and the x–y plane are shown in figure 1. The flow along the z direction behaves somewhat like a Poiseuille flow while the flow in x resembles a $\phi = 0^\circ$ flow described in previous studies of PCP flow. For the strictly laminar case, the flow degenerates to a linear combination of laminar Couette–Poiseuille flow in x and Poiseuille flow in z. The exact solution and several typical profiles are described in Appendix A to illustrate the genuine three-dimensional feature of GCP flow.

Direct numerical simulations with specified (Re, θ, ϕ) are expected to result in a statistically stationary turbulent flow with mean-velocity-profile vector $\boldsymbol{Q} = (U(y), 0, W(y))$. For θ at or near zero, streamwise rolls exist and mean-velocity profiles can be defined that also depend on z, but this description is not considered presently. On the top and bottom walls, the shear stresses will each have vector form in the (x, z) plane that can be expressed in skin-friction coefficient form $\boldsymbol{C_{ft}} = (C_{ft,x}, C_{ft,z})$, $\boldsymbol{C_{fb}} = (C_{fb,x}, C_{fb,z})$ with components

$$C_{ft,x} = \frac{2\nu}{U_0^2}\eta_{t,x}, \quad C_{fb,x} = \frac{2\nu}{U_0^2}\eta_{b,x}, \quad C_{ft,z} = \frac{2\nu}{U_0^2}\eta_{t,z}, \quad C_{fb,z} = \frac{2\nu}{U_0^2}\eta_{b,z}, \tag{2.5a–d}$$

where

$$\eta_{t,x} = \left.\frac{\partial U}{\partial y}\right|_t, \quad \eta_{b,x} = \left.\frac{\partial U}{\partial y}\right|_b, \quad \eta_{t,z} = \left.\frac{\partial W}{\partial y}\right|_t, \quad \eta_{b,z} = \left.\frac{\partial W}{\partial y}\right|_b, \tag{2.6a–d}$$

and subscripts t and b refer to the top and bottom walls, respectively. These can also be expressed in polar form with magnitude and angle

$$C_{ft} = \sqrt{C_{ft,x}^2 + C_{ft,z}^2}, \quad \psi_t = \arctan\left(\frac{C_{ft,z}}{C_{ft,x}}\right), \quad \psi_t \in [0^\circ, 180^\circ], \tag{2.7a,b}$$

where ψ_t measures the angle between $\boldsymbol{C_{ft}}$ and the positive x direction. Similarly, on the bottom wall,

$$C_{fb} = \sqrt{C_{fb,x}^2 + C_{fb,z}^2}, \quad \psi_b = \arctan\left(\frac{C_{fb,z}}{C_{fb,x}}\right), \quad \psi_b \in [0^\circ, 180^\circ]. \tag{2.8a,b}$$

It is expected that when $\phi = 0^\circ$, C_{ft} and C_{fb} reduce to $C_{ft,x}$ and $C_{fb,x}$, respectively. Cheng *et al.* (2023) define $C_{fb,x} > 0$ for Couette-type flow and $C_{fb,x} < 0$ for Poiseuille-type flow. Here there exists a special case with zero velocity gradient on the bottom wall (Coleman *et al.* 2017) so that $C_{fb} = C_{fb,x} = 0$ at a critical angle $\theta = \theta_t(Re)$. It will be seen that flows with $C_{bt,x} = 0$ can be realized for non-zero ϕ but a resultant $C_{fb} = 0$ exists only for $\phi = 0^\circ$, which is parallel Couette–Poiseuille flow. All present GCP flows have $C_{ft} > 0$.

We describe the mean-flow velocity $\boldsymbol{Q}(y)$ by its magnitude $Q(y)$ and angle $\psi_q(y)$ with respect to the x axis as

$$Q = (U^2 + W^2)^{1/2}, \quad \psi_q = \arctan\left(\frac{W}{U}\right), \quad \psi_q \in [0^\circ, 180^\circ]. \tag{2.9a,b}$$

The resultant velocity vectors in the top- and bottom-wall reference frames can be defined as $\boldsymbol{Q_t}(y) = \boldsymbol{Q}(y) + (U_c, 0, 0)$ and $\boldsymbol{Q_b}(y) = \boldsymbol{Q}(y) - (U_c, 0, 0)$, respectively.

The corresponding magnitudes and angles are given by

$$\left.\begin{aligned} Q_t(y) &= \sqrt{(U(y)+U_c)^2+W^2(y)}, \quad \psi_{q,t}(y) = \arctan\frac{W(y)}{U(y)+U_c}, \\ Q_b(y) &= \sqrt{(U(y)-U_c)^2+W^2(y)}, \quad \psi_{q,b}(y) = \arctan\frac{W(y)}{U(y)-U_c}. \end{aligned}\right\} \tag{2.10}$$

We note, for consistency, that in the respective wall-stationary reference frames $\psi_{q,t}(-h) = \psi_t$ and $\psi_{q,b}(h) = \psi_b$.

The present DNS is implemented in terms of specified (Re, θ, ϕ) corresponding to a global Reynolds number and specified volume-flow Reynolds numbers. The mean pressure-gradient vector is then a derived quantity. Its components in the (x, z) directions, $\partial P/\partial x$ and $\partial P/\partial z$, can be obtained by time averages of the volume-integrated, wall-parallel momentum equations. In particular, the magnitude dP/dr and the orientation of the mean pressure-gradient vector ϕ_P with respect to the x axis are then given by

$$\frac{\mathrm{d}P}{\mathrm{d}r} = \sqrt{\left(\frac{\partial P}{\partial x}\right)^2+\left(\frac{\partial P}{\partial z}\right)^2}, \quad \phi_P(Re,\theta,\phi) = \arctan\left(\frac{\partial P}{\partial z}\Big/\frac{\partial P}{\partial x}\right) = \frac{\eta_{z,t}+\eta_{z,b}}{\eta_{x,t}+\eta_{x,b}}. \tag{2.11a,b}$$

For $\phi = 0^\circ,\ \phi = 90^\circ$, then $\phi_P = \phi$ but generally $\phi_P \neq \phi$.

2.2. *Numerical methods and simulations performed*

The DNS is performed by solving the incompressible Navier–Stokes equations

$$\frac{\partial u_i}{\partial x_i} = 0, \quad \frac{\partial u_i}{\partial t}+\frac{\partial u_i u_j}{\partial x_j} = -\frac{\partial p}{\partial x_i}+\nu\frac{\partial^2 u_i}{\partial x_j^2}, \tag{2.12a,b}$$

within a box domain. Here p is the instantaneous pressure divided by the constant fluid density. Boundary conditions in the x and z directions are spatially periodic, while Dirichlet boundary conditions $(u, v, w) = (U_c, 0, 0)$ at $y = -h$ and $(u, v, w) = (-U_c, 0, 0)$ at $y = h$ are used.

A third-order Runge–Kutta time marching technique is implemented combined with the fractional-step method to solve the equations. Conservation of kinetic energy is guaranteed using a staggered-grid strategy employing the skew-symmetric form of the convection term. The Fourier expansions in the x and z directions simplify the pressure-Poisson equation to a series of one-dimensional (1-D) linear Helmholtz equations while a dynamically adjusted time step of δt satisfies the Courant–Friedrichs–Lewy condition. The overall numerical method has been validated by Cheng *et al.* (2023). The spatial domain $L_x \times L_y \times L_z = 8\pi \times 2 \times 8\pi$, with corresponding grid $1536 \times 160 \times 1536$, is square in the $(x$–$z)$ plane owing to the presence of mean flow in both directions. A grid stretching strategy is adopted in the wall-normal direction as proposed by Cheng *et al.* (2022).

Cases implemented are shown as symbols in figure 2(a) within the spherical coordinate system (Re, θ, ϕ). All lie on the surface of the sphere $Re = 6000$ with uniform distribution in (θ, ϕ) with an increment of 15° in the range of $[0^\circ, 90^\circ]$. When $\theta = 0^\circ$, the total volume-flow rate is zero and the flow degenerates to a pure turbulent Couette flow in the x direction.

(*a*)

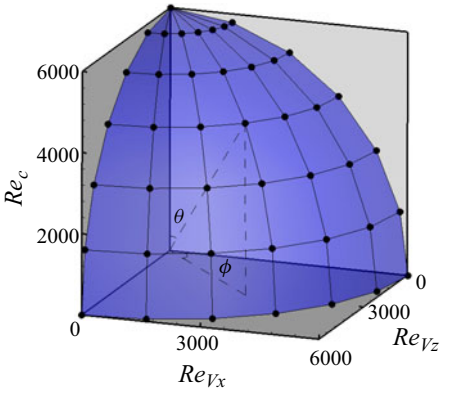

(*b*)

ϕ	$Re_{\tau,t,max}$	$Re_{\tau,b,max}$	Δx^+_{max}	$\Delta y^+_{w,max}$
0°	349.85	441.16	7.21	0.096
15°	358.33	440.33	7.21	0.12
30°	360.43	433.42	7.09	0.12
45°	356.52	414.77	6.78	0.11
60°	351.87	388.10	6.35	0.11
75°	346.82	360.28	5.90	0.098
90°	345.44	345.84	5.66	0.094

Figure 2. (*a*) Cases in spherical coordinates, with radius Re, polar angle θ and azimuthal angle ϕ. All DNS have $Re = 6000$. (*b*) Summary of simulation parameters. Here Re_τ is the friction Reynolds number, Δx^+ is the dimensionless spacing in the x direction and Δy^+_w is the dimensionless spacing at both walls in the y (wall-normal) direction. The subscripts t and b refer to the top and bottom walls, respectively, while the subscript max refers to the maximum value across the range of θ cases at the particular ϕ.

We also list some skin-friction-scaled flow parameters for cases in the table denoted figure 2(*b*). For every ϕ, the maximum values for the skin-friction Reynolds number (defined below) are shown, and also the maximum dimensionless grid spacings, which are based on the skin-friction velocities. The relevant skin-friction velocities are defined by

$$\left.\begin{aligned} u_{\tau,t} &= \mathrm{sgn}(-\eta_{t,x})\sqrt{\nu|\eta_{t,x}|}, \quad u_{\tau,b} = \mathrm{sgn}(\eta_{b,x})\sqrt{\nu|\eta_{b,x}|}, \\ w_{\tau,t} &= \mathrm{sgn}(-\eta_{t,z})\sqrt{\nu|\eta_{t,z}|}, \quad w_{\tau,b} = \mathrm{sgn}(\eta_{b,z})\sqrt{\nu|\eta_{b,z}|}. \end{aligned}\right\} \tag{2.13}$$

Resultant skin-friction speeds can then be expressed as

$$q_{\tau,t} = \mathrm{sgn}(u_{\tau,t})\sqrt{(u^2_{\tau,t} + w^2_{\tau,t})}, \quad q_{\tau,b} = \mathrm{sgn}(u_{\tau,b})\sqrt{(u^2_{\tau,b} + w^2_{\tau,b})}. \tag{2.14a,b}$$

Skin-friction Reynolds numbers and the dimensionless grid spacings on the top wall can be obtained as

$$Re_{\tau,t} = \frac{q_{\tau,t}h}{\nu}, \quad \Delta x^+_t = \frac{\Delta x q_{\tau,t}}{\nu}, \quad \Delta y^+_{w,t} = \frac{\Delta y_w q_{\tau,t}}{\nu}, \quad \Delta z^+_t = \frac{\Delta z q_{\tau,t}}{\nu}. \tag{2.15a–d}$$

Quantities on the bottom wall, including $Re_{\tau,b}$, Δx^+_b, $\Delta y^+_{w,b}$, Δz^+_b, can be similarly defined. Tabulated values in figure 2(*b*) are for all cases with the particular ϕ shown. These indicate that the present DNS generally meets accepted criteria for pointwise convergence with respect to grid size. For example, the in-plane resolution is comparable to both Pirozzoli *et al.* (2014) and Lee & Moser (2018).

3. Orthogonal Couette–Poiseuille flow: $\phi = 90°$

In Cheng *et al.* (2023), unsymmetric flow with $\phi = 0°$ shows three interesting flow regimes, two of which comprise Couette-type flow in $0 \le \theta < \theta_c$ and Poiseuille-type in $\theta_c < \theta \le 90°$, where θ_c is the angle for which the shear stress on the bottom wall vanishes. A third regime consists of all flows with varying Re for which the bottom-wall

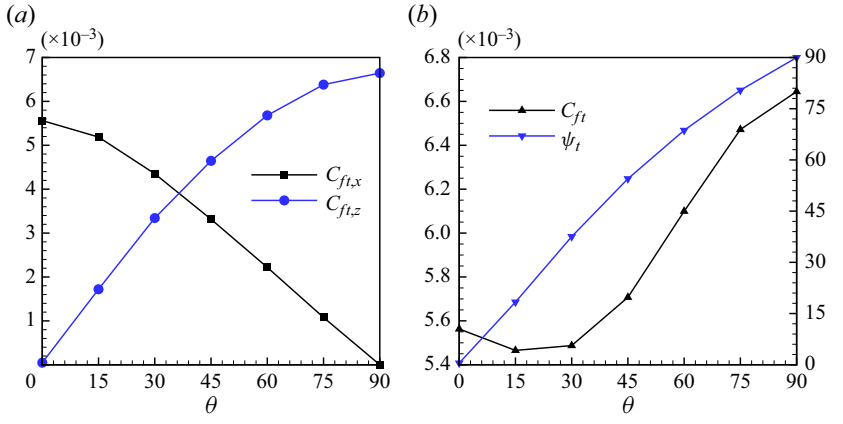

Figure 3. Components of the skin-friction vector on the top wall for OCP flow with $\phi = 90°$. (*a*) In Cartesian coordinates ($C_{ft,x}$, $C_{ft,z}$). The black line is the skin-friction coefficient $C_{ft,x}$ in the x direction, while the blue line is the skin-friction coefficient $C_{ft,z}$ in the z direction. (*b*) In polar coordinates (C_{ft}, ψ_t). The black line is the magnitude C_{ft} calibrated by the left coordinate axis, while the blue line is the twist angle ψ_t calibrated by the right axis.

shear stress vanishes. Orthogonal Couette–Poiseuille flow with $\phi = 90°$ shows a central symmetry, and is another useful limit. Here the flow in the x direction is of Couette type while the z direction flow is pressure-driven giving Poiseuille-type flow. Mean-velocity profiles satisfy symmetries $U(y) = -U(-y)$ and $W(y) = W(-y)$. In the following analysis we consider flow parameters in the top half-channel flow adjacent to the top wall with subscript t. The corresponding bottom half-channel flow can be inferred using symmetry.

3.1. *Skin-friction components*

Figure 3(*a*) shows the skin-friction coefficient components ($C_{ft,x}$, $C_{ft,z}$) while figure 3(*b*) shows (C_{ft}, ψ_t). Since the top wall moves in the negative x direction, both $C_{ft,x}$ and $C_{ft,z}$ are positive. With increasing θ, $C_{ft,x}$ is reduced as Re_c decreases, while $C_{ft,z}$ increases with the increase of Re_{V_z}. The skin friction in PC flow $\theta = 0°$ is smaller than for PP flow $\theta = 90°$ owing to the definition of Re.

In figure 3(*b*), C_{ft} is the resultant skin friction and $\psi_t = \arccos(C_{ft,x}/C_{ft})$ describes the angle between the top-wall skin-friction vector and the x axis. As θ increases from 0° to 15°, a small decrease of C_{ft} is observed, which can be ascribed to the disappearance of large-scale roll structures observed in pure Couette flow ($\theta = 0$). Further evidence will be discussed in § 6.2. When θ further increases from 15° → 90°, C_{ft} generally increases with an increasing proportion or weighting of Poiseuille-type flow. It is interesting that the curve of ψ_t-θ is convex with $\psi_t > \theta$ except at $\psi_t = \theta = 0°$ for PC flow and $\psi_t = \theta = 90°$ for PP flow where $\psi_t = \theta$. This indicates coupling of the wall surface force and the externally applied pressure gradient for turbulent GCP flow, which is different to that for laminar flow.

3.2. *Velocity profiles*

Mean component velocity profiles scaled in outer variables using U_0 are shown in figure 4. When $\theta = 0°$, the U/U_0 mean-velocity profile conforms to pure Couette flow. As θ increases, $U(y)/U_0$ in figure 4(*a*) decreases with decreasing Re_c eventually to zero

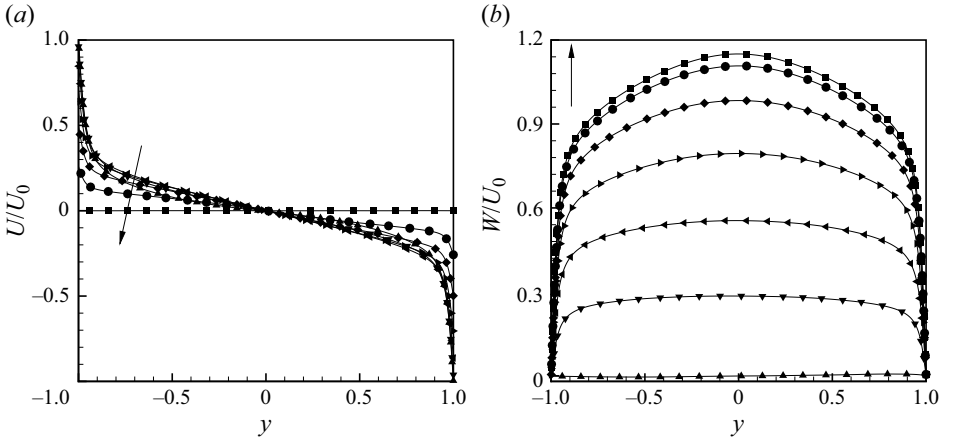

Figure 4. Mean-velocity profiles, $\phi = 90°$: (*a*) U/U_0. (*b*) W/U_0. Key: ▲: $\theta = 0°$, ▼: $\theta = 15°$, ◀: $\theta = 30$, ▶: $\theta = 45°$, ♦: $\theta = 60°$, ●: $\theta = 75°$, ■: $\theta = 90°$. The black arrows indicate increasing θ.

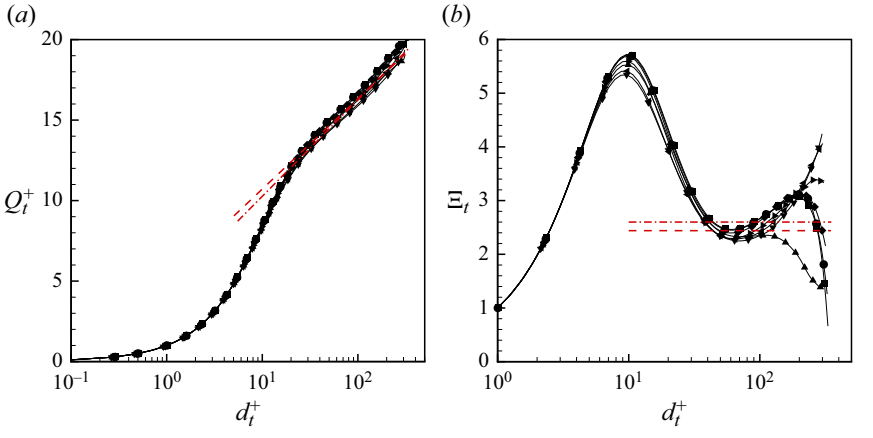

Figure 5. Inner-scaled velocity magnitude for OCP flow, $\phi = 90°$. (*a*) Scaled mean resultant velocity magnitude Q_t^+. Red dashed lines: log law with $\kappa = 0.41$ and $A = 5.1$ for Couette flow; red dash-dotted lines: $\kappa = 0.384, A = 4.27$ for Poiseuille flow. (*b*) Velocity gradient indicator function Ξ_t. Red dashed lines: reference lines of $1/0.41$; red dash-dotted lines: reference lines of $1/0.384$. See figure 4 for symbol key.

for $\theta = 90°$. The mean spanwise velocity profile $W(y)/U_0$ is always symmetric, and approaches pure Poiseuille flow for $\theta = 90°$. As θ increases, the magnitude of $W(y)$ monotonically increases up to $\theta = 90°$, when $Re_V = Re_{Vz}$.

3.2.1. *Mean-flow velocity magnitude $Q(y)$*

The mean-flow velocity always lies in the (x, z) plane but generally displays twist with respect to (x, z) axes and with variation in the y direction. In figure 5(*a*) the velocity magnitude is plotted as Q_t^+ vs d_t^+ with

$$Q_t^+ = \frac{Q_t}{q_{\tau,t}}, \quad d_t^+ = \frac{(h-y)q_{\tau,t}}{\nu}, \tag{3.1a,b}$$

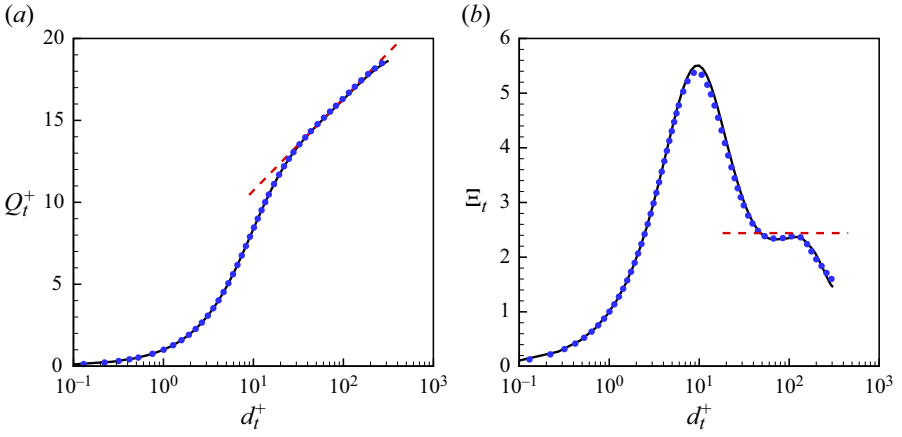

Figure 6. Comparison of mean-velocity profile and indicator function for PC flow ($\phi = 90°, \theta = 0°$) at $Re = 6000$ with Cheng *et al.* (2023). (*a*) Scaled mean resultant velocity magnitude Q_t^+. Dashed line: logarithmic law of $Q_t^+ = \ln d_t^+/0.41 + 5.1$. (*b*) Velocity gradient indicator function Ξ_t. Dashed line: reference line of $1/0.41$. Solid line: present DNS with $L_x \times L_y \times L_z = (8\pi \times 2 \times 8\pi)$. Blue dotted symbols: Cheng *et al.* (2023) with $L_x \times L_y \times L_z = (20\pi \times 2 \times 6\pi)$.

for $\theta = 0°$–$90°(15°)$, where $q_{\tau,t}$ is defined by (2.14*a*,*b*). As θ increases from 0° to 90°, the flow undergoes a change from PC to PP flow, and this is accompanied by some variation in the profiles in the nominal log region. According to some authors, parameters in the standard log law can differ for different canonical flows (Nagib & Chauhan 2008). In figure 5(*a*) the red dashed line is the log profile for PC flow, with $\kappa = 0.41$ and $A = 5.1$ obtained by Pirozzoli *et al.* (2014), while the red dash-dotted line is the component log law for PP flow, with $\kappa = 0.384$ and $A = 4.27$ as found by Lee & Moser (2015). When $\theta = 0°$ (pure Couette flow), Q_t^+ is in good agreement with the log law. When θ increases from 0° to 15°, Q_t^+ first decreases and then increases as θ increases from 15° to 90°. When $\theta = 90°$, the slope of the velocity profile is basically parallel to the reference line of a log law for Poiseuille flow.

The velocity gradient indicator function Ξ_t can be defined as

$$\Xi_t = d_t^+ \frac{\mathrm{d}Q_t^+}{\mathrm{d}d_t^+}. \tag{3.2}$$

This is shown in figure 5(*b*) where there is a broad minimum value of approximately $1/0.41$ near $d_t^+ \approx 60$ when $\theta = 0°$. This is interpreted presently as the onset of a log region. Our present $Re = 6000$ is perhaps not sufficiently large to see this more fully developed. When θ increases, this minimum first drops and then gradually rises.

The present computational domain is relatively shorter in the streamwise (x) direction and wider in the spanwise (z) direction, compared with typical PC flow simulation domains. To verify that the present domain provides accurate mean-velocity profiles, we compare the PC profile with $L_x \times L_y \times L_z = (8\pi \times 2 \times 8\pi)$ at the same Reynolds number $Re = 6000$ with data from Cheng *et al.* (2023) who used a similar computational domain to Lee & Moser (2018), $L_x \times L_y \times L_z = (20\pi \times 2 \times 6\pi)$. As shown in figure 6, both the scaled mean resultant velocity Q_t^+ and the velocity gradient indicator function Ξ_t agree well, providing validity of one-point diagnostics for the present simulations.

3.2.2. *Component mean-flow profiles*

The velocity components in the top-wall reference frame can be expressed in terms of Q_t and the twisting angle $\psi_{q,t}$ as

$$U + U_c = Q_t \cos\psi_{q,t}, \quad W = Q_t \sin\psi_{q,t}, \tag{3.3a,b}$$

while skin-friction velocities are related by

$$u_{\tau,t}^2 = q_{\tau,t}^2 \cos\psi_t, \quad w_{\tau,t}^2 = q_{\tau,t}^2 \sin\psi_t, \tag{3.4a,b}$$

where it is recalled that ψ_t is the skin-friction angle at the wall. At the top wall $\psi_{q,t}(y = h) = \psi_t$ because the mean-flow streamlines are asymptotic to the skin-friction lines when $y \to h$.

We assume that a classical log region exists for $Q_t(y)$:

$$\frac{Q_t}{q_{\tau,t}} = \frac{1}{\kappa} \ln\left(\frac{d_t q_{\tau,t}}{\nu}\right) + A. \tag{3.5}$$

We further make the approximation that the velocity-profile twist angle is constant and equal to its value at the wall, $\psi_{q,t}(y) = \psi_t$. This will be discussed later. From (3.3*a*,*b*), (3.4*a*,*b*) and (3.5) we can then obtain

$$U_t^+ = \frac{\sqrt{\cos\psi_t}}{\kappa} \ln d_{x,t}^+ + \sqrt{\cos\psi_t}\left(A - \frac{\ln\sqrt{\cos\psi_t}}{\kappa}\right), \tag{3.6}$$

$$W_t^+ = \frac{\sqrt{\sin\psi_t}}{\kappa} \ln d_{z,t}^+ + \sqrt{\sin\psi_t}\left(A - \frac{\ln\sqrt{\sin\psi_t}}{\kappa}\right), \tag{3.7}$$

where

$$U_t^+ = \frac{U + U_c}{u_{\tau,t}}, \quad W_t^+ = \frac{W}{w_{\tau,t}}, \quad d_{x,t}^+ = \frac{(h-y)u_{\tau,t}}{\nu}, \quad d_{z,t}^+ = \frac{(h-y)w_{\tau,t}}{\nu}. \tag{3.8a–d}$$

These are referred to as modified component log relations.

Figure 7 shows mean-velocity components U_t^+ and W_t^+ scaled with $u_{\tau,t}$ and $w_{\tau,t}$, respectively, obtained from the DNS, each for $\theta = 0°$–$90°(15°)$. Also shown are red lines representing (3.6) and (3.7). These each use $(u_{\tau,t}, w_{\tau,t})$ and $\psi_{q,t} = \psi_t$ obtained from the DNS for the various θ values. In figure 7(*a*) the red dashed lines are plotted with $\kappa = 0.41$ and $A = 5.1$ as discussed above for PC flow while in figure 7(*b*) the red dash-dotted lines are plotted with $\kappa = 0.384$ and $A = 4.27$ for PP flow.

In summary, the velocity magnitude exhibits a log region albeit, for the present $Re = 6000$, with standard parameters that show a weak dependence on θ as the flow changes from Couette-like to Poiseuille-like as θ increases. The component mean-velocity profiles also exhibit log-like regimes with parameters that can be well estimated by approximating the mean-velocity angle of twist as the shear-stress angle at the wall in the reference frame where the wall is stationary.

4. Mean-flow modelling

The above analysis of the relation between the geometry of the resultant mean-flow velocity and the component modified log relations for the OCP turbulent flows suggests an approach to empirical modelling for GCP flows. This is now developed. For the purpose of clarity, it will be convenient to work in terms of Re_τ in lieu of C_f. These parameters

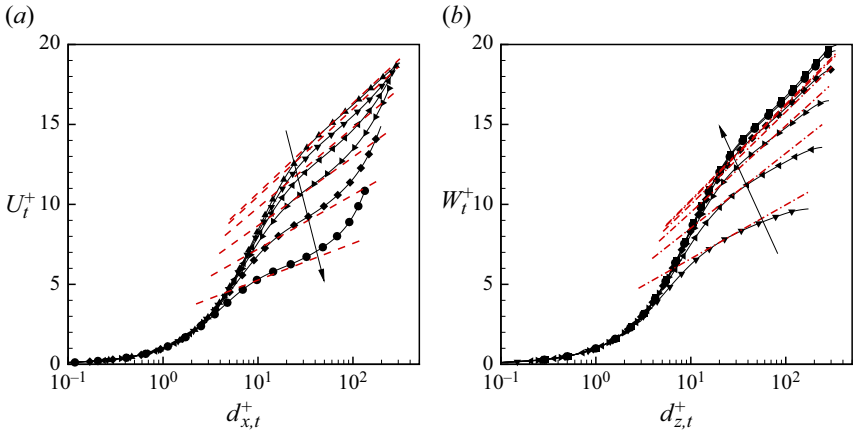

Figure 7. Mean-velocity components in the top-wall reference frame scaled with $u_{\tau,t}$ and $w_{\tau,t}$ for OCP flow with $\phi = 90°$. Plots of (*a*) U_t^+ vs $d_{x,t}^+$ and (*b*) W_t^+ vs $d_{z,t}^+$. See figure 4 for symbol key. The black arrows indicate increasing θ.

satisfy $C_f = 2Re_\tau^2/Re^2$ for both walls. Cheng *et al.* (2023) developed mean-flow empirical modelling of PCP flow ($\phi = 0°$) finding satisfactory agreement between calculated top/bottom-wall skin-friction coefficients and values obtained from DNS up to $Re = 6000$, wall-resolved LES up to $Re = 20\,000$ and wall-modelled LES to $Re = 10^{10}$ over $0° \leq \theta \leq 90°$. Furthermore, the model was able to accurately capture the transition from PC-type flow to PP-type flow, when the bottom-wall skin friction changes sign at a critical $\theta = \theta_c(Re)$. The above suggests the extension of the PCP modelling approach to GCP turbulent flows within the parameter space (Re, θ, ϕ). We thus seek to predict the dependence of (C_{ft}, ψ_t), (C_{fb}, ψ_b) on (Re, θ, ϕ). Since the z-direction flow always shows Poiseuille-like behaviour while the x flow is of a mixed Couette–Poiseuille type, it is necessary to discuss two different flow regimes. Following Cheng *et al.* (2023), the first is Couette-type flow defined as $C_{fb,x} < 0$ that corresponds to $90° \leq \psi_b \leq 180°$. Here $U(y)$ is not expected to show an interior maximum, and use of simple log-type profiles, without wake components (small for Couette flow) suffice. An interior maximum is expected for the Poiseuille-type $W(y)$ profile. This requires a more refined mean-flow model to be described. The second regime is for Poiseuille-type flow defined as $C_{fb,x} > 0$, equivalent to $0° \leq \psi_b \leq 90°$. Both $U(y)$ and $W(y)$ are then expected to have interior maxima.

The following model development employs empirical log profiles and is thus considered a high-Re approximation. While our present $Re = 6000$ is perhaps not sufficiently large to display a fully developed log region, the model will nonetheless be shown to reproduce the variation of several flow diagnostics with (θ, ϕ). In numerical model calculations the possible distinction between PP and PC flows is ignored and the nominal values $\kappa = 0.4$, $A = 5.0$, $\Pi = 0.2$ are utilized where Π is the Coles wake parameter.

4.1. *Couette-type flow* $90° \leq \psi_b \leq 180°$

Uppercase U and W denote model mean-velocity profiles in the laboratory reference frame. For Couette-type flow, we assume that the composite $U(y)$ mean-velocity profile comprises two pure log profiles relative to respective top and bottom walls, and then each transformed to the laboratory frame. These then join at a location $y = y_0$ to be determined. In the laboratory framework, the bottom-adjacent and top-adjacent profiles can then be

expressed as

$$\mathrm{I}: -h < y \le y_0 : U(y) = U_c - q_{\tau,b}\cos\psi_b\left(\frac{1}{\kappa}\ln\left(\frac{(h+y)|q_{\tau,b}|}{\nu}\right)+A\right), \tag{4.1}$$

$$\mathrm{II}: y_0 \le y < h : U(y) = -U_c + q_{\tau,t}\cos\psi_t\left(\frac{1}{\kappa}\ln\left(\frac{(h-y)q_{\tau,t}}{\nu}\right)+A\right), \tag{4.2}$$

where κ is the Kármán parameter and A the offset constant.

For $W(y)$, we use the modelling profiles of Jones, Marusic & Perry (2001) that here take the form

$$\mathrm{III}: -h < y \le y_1 : W(y) = -q_{\tau,b}\sin\psi_b\left[\frac{1}{\kappa}\ln\left(\frac{(h+y)|q_{\tau,b}|}{\nu}\right)+A - \frac{1}{3\kappa}\left(\frac{h+y}{h+y_1}\right)^3 + 2\frac{\Pi}{\kappa}\left(\frac{h+y}{h+y_1}\right)^2\left(3-2\frac{h+y}{h+y_1}\right)\right], \tag{4.3}$$

$$\mathrm{IV}: y_1 < y \le h : W(y) = q_{\tau,t}\sin\psi_t\left[\frac{1}{\kappa}\ln\left(\frac{(h-y)q_{\tau,t}}{\nu}\right)+A - \frac{1}{3\kappa}\left(\frac{h-y}{h-y_1}\right)^3 + 2\frac{\Pi}{\kappa}\left(\frac{h-y}{h-y_1}\right)^2\left(3-2\frac{h-y}{h-y_1}\right)\right]. \tag{4.4}$$

In the interests of constructing a relatively simple model, refinements such as pressure-gradient corrections in the wake function (Luchini 2018) have not been implemented. The two profiles join at the interior maximum point $y = y_1$, to be determined, where both have zero slope by construction. Cheng *et al.* (2023) found that this model profile worked well for $\phi = 0^\circ$ except near $\theta - \theta_c$ small but non-zero where the flow near the bottom wall relaminarizes, before, as θ increases, transitioning back to turbulence. Since this effect is expected to be limited to a small region of $(\theta - \phi)$ space near $\theta = \theta_c$ and small ϕ, and to shrink with increasing Re, then this is presently neglected.

When expressed in terms of Reynolds numbers, with (Re, θ, ϕ) given, there are six unknowns: $Re_{\tau,b}$, ψ_b, $Re_{\tau,t}$, ψ_t, y_0/h and y_1/h. Four equations are obtained from matching $U(y)$ and $\mathrm{d}U/\mathrm{d}y$ at $y = y_0$, $W(y)$ and $\mathrm{d}^2W/\mathrm{d}y^2$ at $y = y_1$ using the above profiles:

$$U(y \to y_0^-) = U(y \to y_0^+), \quad \left.\frac{\mathrm{d}U}{\mathrm{d}y}\right|_{y_0\to y_0^-} = \left.\frac{\mathrm{d}U}{\mathrm{d}y}\right|_{y\to y_0^+}, \tag{4.5a,b}$$

$$W(y \to y_1^-) = W(y \to y_1^+), \quad \left.\frac{\mathrm{d}^2W}{\mathrm{d}y^2}\right|_{y\to y_1^-} = \left.\frac{\mathrm{d}^2W}{\mathrm{d}y^2}\right|_{y\to y_1^+}. \tag{4.6a,b}$$

These give, respectively, after some algebra,

$$2\kappa Re\cos\theta - A\kappa(Re_{\tau,b}\cos\psi_b + Re_{\tau,t}\cos\psi_t) - Re_{\tau,b}\cos\psi_b\ln(|Re_{\tau,b}|(1+Y_0)) - Re_{\tau,t}\cos\psi_t\ln(Re_{\tau,t}(1-Y_0)) = 0, \tag{4.7}$$

$$Re_{\tau,b}\sin\psi_b[3AK + 6P + 3\ln(|Re_{\tau,b}|(Y_1+1)) - 1] + [3AK + 6P + 3\ln(Re_{\tau,t}(1-Y1)) - 1]Re_{\tau,t}\sin\psi_t = 0, \tag{4.8}$$

$$Y_0 = \frac{Re_{\tau,b}\cos\psi_b - Re_{\tau,t}\cos\psi_t}{Re_{\tau,b}\cos\psi_b + Re_{\tau,t}\cos\psi_t}, \tag{4.9}$$

$$Y_1 = \frac{\sqrt{|Re_{\tau,b}|\sin\psi_b} - \sqrt{Re_{\tau,t}\sin\psi_t}}{\sqrt{|Re_{\tau,b}|\sin\psi_b} + \sqrt{Re_{\tau,t}\sin\psi_t}}, \tag{4.10}$$

where $Y_0 = y_0/h$ and $Y_1 = y_1/h$. Two further closing equations are obtained by substituting (4.1), (4.2), (4.3) and (4.4) into (2.1*a*,*b*) to give $Re_{Vx} \equiv Re\sin\theta\cos\phi$ and $Re_{Vz} \equiv Re\sin\theta\sin\phi$. The mass-flux integration can be done and the resulting equations, with Re, θ and ϕ given, are

$$2\kappa Re(\sin\theta\cos\phi - Y_0\cos\theta) + Re_{\tau,b}(Y_0+1)\cos\psi_b(A\kappa + \ln(|Re_{\tau,b}|(1+Y_0)) - 1) + Re_{\tau,t}(Y_0-1)\cos\psi_t(A\kappa + \ln(Re_{\tau,t}(1-Y_0)) - 1) = 0, \tag{4.11}$$

$$24\kappa Re\sin\phi\sin\theta + Re_{\tau,b}(Y_1+1)\sin\psi_b(12A\kappa + 12P + 12\ln(|Re_{\tau,b}|(Y_1+1)) - 13) + Re_{\tau,t}(Y_1-1)\sin\psi_t(12A\kappa + 12P + 12\ln(Re_{\tau,t}(1-Y_1)) - 13) = 0. \tag{4.12}$$

Equations (4.7)–(4.12) describe Couette-type flow with $Re_{\tau,x,b} < 0$. Near-wall viscous sublayer regions can be included at the cost of additional complexity, but the effect is negligibly small at values of Re presently considered, even for near-bottom-wall flow when $|Re_{\tau,b}|$ is small.

For $\theta = 0$, these equations have the exact solution $Re_{\tau,b} = -Re_{\tau,t}$, $Y_0 = 0$ and

$$Re_{\tau,t} = \frac{\kappa Re}{W(\mathrm{e}^{A\kappa}\kappa Re)}, \tag{4.13}$$

corresponding to pure Couette flow, where $W(Z)$ is the ProductLog function or Lambert function, which is the solution of $Z = W\ln(W)$. For given Re, θ and ϕ, the six equations must generally be solved numerically with validity extended to $\psi_b = 90°$, which is the limit of Couette-type flow in the streamwise direction.

4.2. *Poiseuille-type flow* $0° \le \psi_b \le 90°$

In this regime, all model profiles take the Jones *et al.* (2001) log-wake form

$$\mathrm{I}: -h < y \le y_0 : U(y) = U_c + q_{\tau,b}\cos\psi_b\left[\frac{1}{\kappa}\ln\left(\frac{(h+y)q_{\tau,b}}{\nu}\right) + A - \frac{1}{3\kappa}\left(\frac{h+y}{h+y_0}\right)^3 + 2\frac{\Pi}{\kappa}\left(\frac{h+y}{h+y_0}\right)^2\left(3 - 2\frac{h+y}{h+y_0}\right)\right], \tag{4.14}$$

$$\mathrm{II}: y_0 \le y < h : U(y) = -U_c + q_{\tau,t}\cos\psi_t\left[\frac{1}{\kappa}\ln\left(\frac{(h-y)q_{\tau,t}}{\nu}\right) + A - \frac{1}{3\kappa}\left(\frac{h-y}{h-y_0}\right)^3 + 2\frac{\Pi}{\kappa}\left(\frac{h-y}{h-y_0}\right)^2\left(3 - 2\frac{h-y}{h-y_0}\right)\right], \tag{4.15}$$

$$\text{III}: -h < y \le y_1 : W(y) = q_{\tau,b} \sin\psi_b \left[\frac{1}{\kappa} \ln\left(\frac{(h+y)q_{\tau,b}}{\nu} \right) + A \right.$$
$$\left. - \frac{1}{3\kappa} \left(\frac{h+y}{h+y_1} \right)^3 + 2\frac{\Pi}{\kappa} \left(\frac{h+y}{h+y_1} \right)^2 \left(3 - 2\frac{h+y}{h+y_1} \right) \right], \tag{4.16}$$

$$\text{IV}: y_1 < y \le h : W(y) = q_{\tau,t} \sin\psi_t \left[\frac{1}{\kappa} \ln\left(\frac{(h-y)q_{\tau,t}}{\nu} \right) + A \right.$$
$$\left. - \frac{1}{3\kappa} \left(\frac{h-y}{h-y_1} \right)^3 + 2\frac{\Pi}{\kappa} \left(\frac{h-y}{h-y_1} \right)^2 \left(3 - 2\frac{h-y}{h-y_1} \right) \right], \tag{4.17}$$

and zero slope is automatic in both $U(y)$ and $W(y)$ profiles at $Y = Y_0, Y = Y_1$, respectively.

The velocity matching conditions for $U(y)$ and $W(y)$ are still $U(y \to y_0^-) = U(y \to y_0^+)$ and $W(y \to y_1^-) = W(y \to y_1^+)$, while the second-derivative matching conditions are now

$$\left.\frac{\mathrm{d}^2U}{\mathrm{d}y^2}\right|_{y\to y_0^-} = \left.\frac{\mathrm{d}^2U}{\mathrm{d}y^2}\right|_{y\to y_0^+}, \quad \left.\frac{\mathrm{d}^2W}{\mathrm{d}y^2}\right|_{y\to y_1^-} = \left.\frac{\mathrm{d}^2W}{\mathrm{d}y^2}\right|_{y\to y_1^+}. \tag{4.18a,b}$$

Closure equations are again obtained by substituting (4.14), (4.15), (4.16) and (4.17) into (2.1*a*,*b*), and the mass flux integration can be done analytically. Details are omitted. A Poiseuille-type flow model is then obtained with six unknowns and six equations.

Numerical calculations were performed by first fixing $Re = 6000$ (but any large value can be used). For each ϕ, with $\theta = 0^\circ$, the solution strategy begins using the Couette-type model of (4.1). Solutions to the nonlinear equations were obtained numerically in a symbolic environment powered by MATHEMATICA®. As θ increases, the solution angle ψ_b decreases from $\psi_b = 180^\circ$ until, for some θ, a solution with $\psi_b > 90^\circ$ cannot be found. For this θ, there is then a switch to the Poiseuille-type model equations of this section that are utilized until $\theta = 90^\circ$. This process is repeated for all $0 \le \phi \le 90^\circ$ with 2.5° increments. Numerical solutions were found without difficulty for all (ϕ, θ) in the stated ranges. A quite small discontinuity in solution quantities exists in the change from the Couette-type to the Poiseuille-type equations as ψ_b passes through $\psi_b = 90^\circ$, but since this is expected to be smaller than the general accuracy of the model, it is ignored.

For $\theta = 90^\circ$, the equations have $Re_{\tau,b} = Re_{\tau,t}$, $Y_0 = Y_1 = 0$ and

$$Re_{\tau,t} = \frac{\kappa Re}{W(\exp(-13/12 + \Pi + A\kappa)\kappa Re)}, \tag{4.19}$$

corresponding to pure Poiseuille flow.

5. Generalized Couette–Poiseuille flow

5.1. *Skin-friction components*

Modelling results are calculated as described above, and then converted to skin-friction coefficients. Figure 8 shows the distributions of $C_{fb,x}$, $C_{fb,z}$, $C_{ft,x}$ and $C_{ft,z}$. Each red point denotes a DNS result while the blue surface is fitted to the model calculations. When $\theta = 0^\circ$, the seven points contract to a single PC flow. Figure 8(*a*) shows $C_{fb,x}$ on the bottom wall. With $\theta = 0^\circ$, $C_{fb,x} < 0$ for PC flow. When θ increases, $C_{fb,x}$ crosses zero

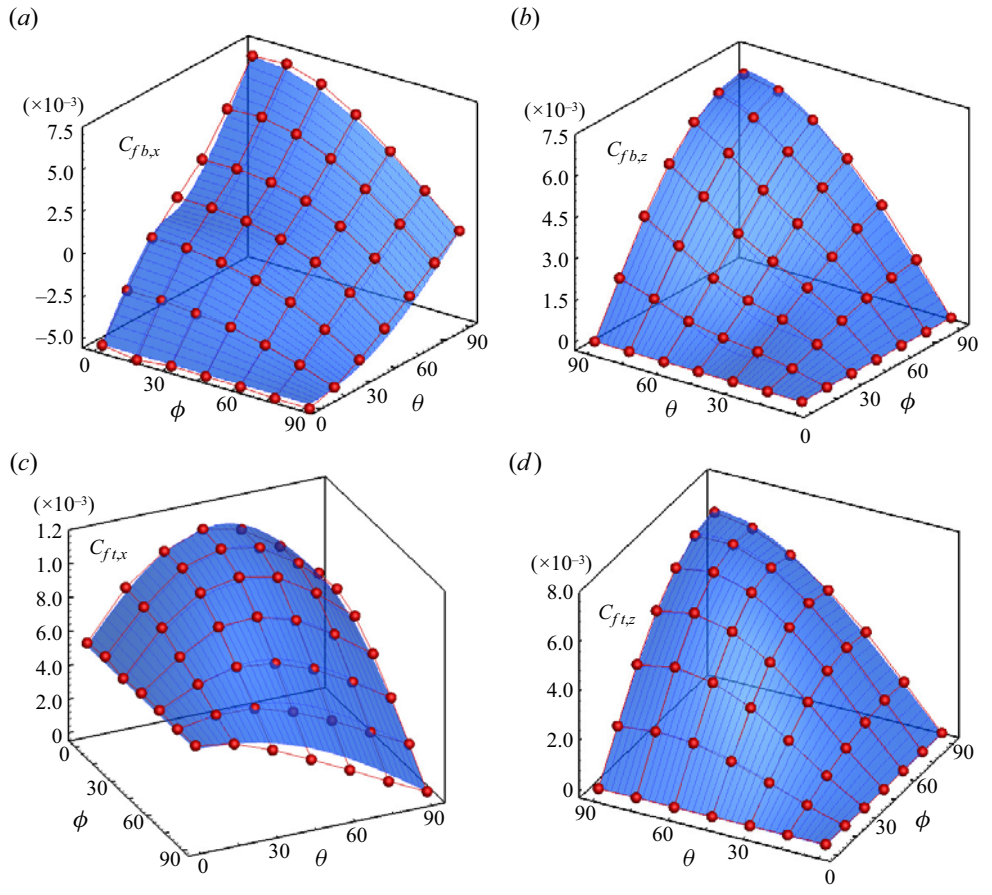

Figure 8. Components of skin-friction coefficients in Cartesian coordinates. Red spherical points are from DNS at $Re = 6000$. The blue is a surface fitted to model calculations with fine resolution in $(\theta - \phi)$ variables. Results are shown for (*a*) $C_{fb,x}$, (*b*) $C_{fb,z}$, (*c*) $C_{ft,x}$, (*d*) $C_{ft,z}$.

at a critical angle $\theta = \theta_c(\phi) \approx 37.5^\circ$. For $\theta > \theta_c$, $C_{fb,x} > 0$ and increases with increasing θ. Following Cheng *et al.* (2023), we define flow with $C_{fb,x} < 0$ as Couette type and the flow with $C_{fb,x} > 0$ as Poiseuille type. Figure 8(*c*) shows $C_{ft,x} > 0$. When $\phi \neq 90^\circ$, the x flow is driven by both moving walls and the x component of the pressure gradient. With increasing θ, $C_{ft,x}$ first increases and then decreases, consistent with the results of $Re_{\tau,t}$ in Cheng *et al.* (2023). This is not the case for $\phi = 90^\circ$, which shows a monotonic decrease in figure 3. Figure 8(*b*,*d*) shows z skin-friction components. When either ϕ or θ gradually increase, both $C_{fb,z}$ and $C_{ft,z}$ increase with increasing volume flow in the z direction. The modelling generally well predicts the trend of all these skin-friction components in the (ϕ, θ) plane.

Figure 9 shows the skin friction at both walls in polar coordinates (C_{fb}, ψ_b) and (C_{ft}, ψ_t). Symbols are DNS at discrete (ϕ, θ), while the dashed lines are the corresponding model predictions. Figure 9(*a*) shows the skin-friction coefficient C_{fb} on the bottom wall. For flows with small ϕ, when θ is increased, C_{fb} first decreases from the value for PC flow to a minimum, as a result of flow laminarization on the bottom wall near $\theta = \theta_c$ (Cheng *et al.* 2023), and then increases to the PP limit. In contrast, on the top wall in figure 9(*c*), C_{ft} first increases from the pure Couette–Poiseuille flow value to a maximum, and then decreases

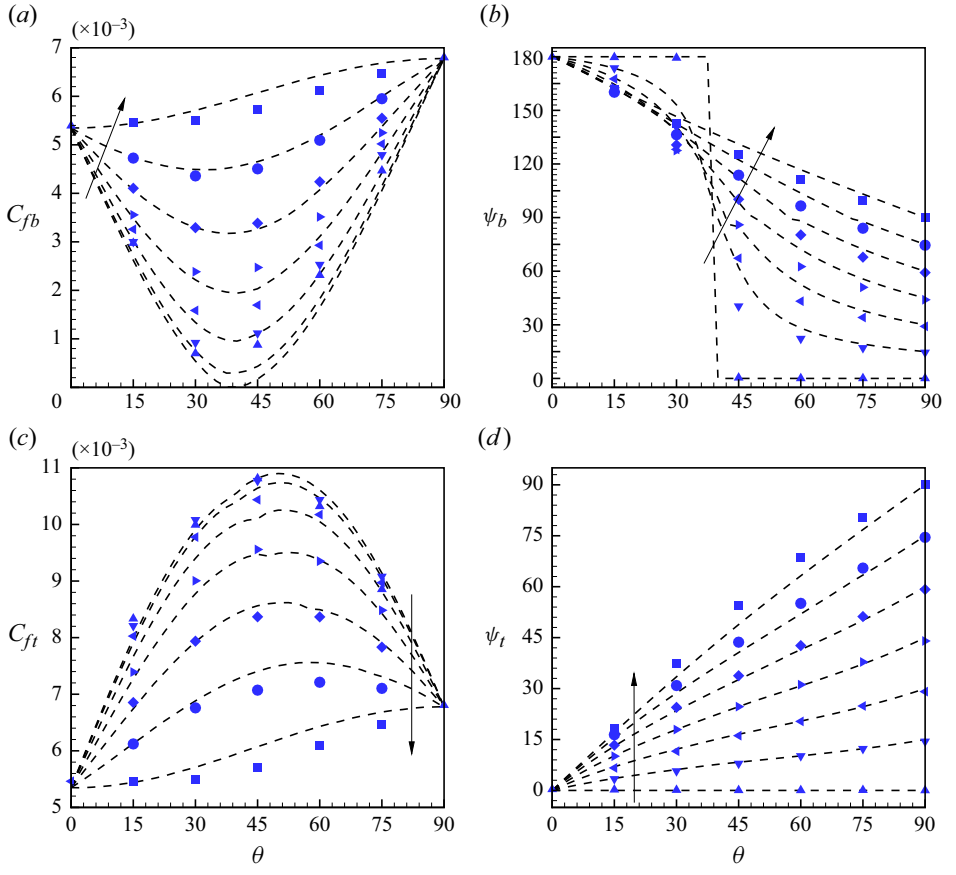

Figure 9. Skin friction in polar coordinates for both walls versus θ for different ϕ. Filled symbols are from DNS and the dashed lines are the model results. Results are shown for (*a*) C_{fb}, (*b*) ψ_b, (*c*) C_{ft}, (*d*) ψ_t. Note that for $\theta = 90°$, both ψ_b, $\psi_t \to \phi$. Key: (▲, blue): $\phi = 0°$, (▼, blue): $\phi = 15°$, (◀, blue): $\phi = 30$, (▶, blue): $\phi = 45°$, (◆, blue): $\phi = 60°$, (●, blue): $\phi = 75°$, (■, blue): $\phi = 90°$. The black arrows indicate increasing ϕ.

to pure Poiseuille flow as θ is increased, which is also consistent with the behaviour of $Re_{\tau,t}$ in Cheng *et al.* (2023). The limit $\theta \to 90°$ corresponds to pure Poiseuille flow in the direction defined by ϕ. Here ψ_b, $\psi_t \to \phi$, which is captured by both the DNS and the mean-flow model. There are quantitative discrepancies between the modelling and DNS for some components of C_f over parts of (θ, ϕ) space, which are attributable both to flow relaminarization near $\theta = \theta_c$, $\phi = 0$ (not included in the model but implemented in Cheng *et al.* 2023), and also to the fact that the model is a large-Reynolds-number approximation. But overall the modelling well captures the general trend of the DNS. The orientation angles (ψ_b, ψ_t) are shown in figure 9(*b*,*d*), respectively. When $\phi = 0°$, we have PCP flow, where on the bottom wall at $\theta = \theta_c$, ψ_b changes discontinuously from 180° to 0°. When $\phi \neq 0°$, the flow changes from PC-type flow to PP-type flow smoothly when $\psi_b = 90°$ at an angle θ that depends on ϕ and that can be determined from figure 9(*b*).

The DNS method fixes the volume-flow vector and not the mean pressure-gradient vector. Volume–time integration of (2.11*a*,*b*) shows that the resultant skin-friction forces are balanced by the mean pressure gradient. Figure 10 shows both the magnitude and direction ϕ_p of the mean pressure gradient, where the latter can be calculated using (2.11*a*,*b*). In pure Couette flow with $\theta = 0°$, there is a zero pressure gradient. When θ

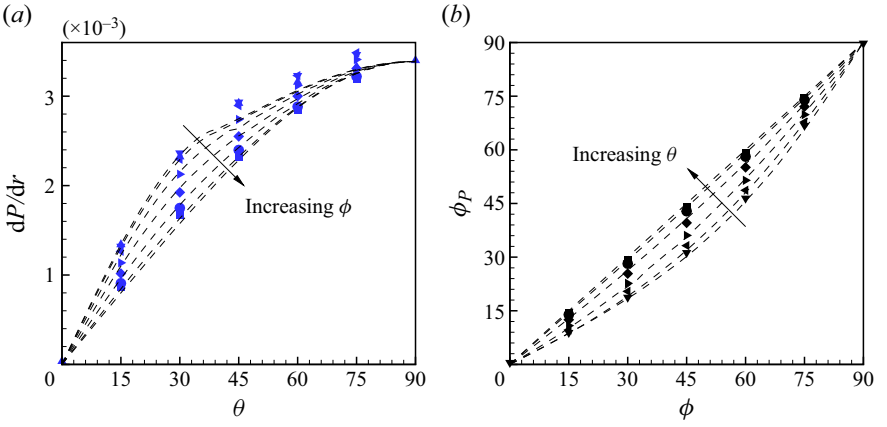

Figure 10. Magnitude and angle ϕ_P of the mean pressure-gradient vector. Filled symbols for DNS and dashed lines for model calculations. (*a*) Plot of $\mathrm{d}P/\mathrm{d}r$ vs θ; see figure 9 for symbol key. (*b*) Plot of ϕ_P vs θ; see figure 4 for symbol key.

increases, $\mathrm{d}P/\mathrm{d}r$ increases with the growing proportion of Poiseuille flow, and reaches a maximum value at $\theta = 90^\circ$. Except for relaminarization near $\theta = \theta_c$, the model captures the general trend of the DNS results. If Couette flow and Poiseuille flow are decoupled, as for laminar flow, the pressure-gradient vector is parallel to the mass-flow direction defined by ϕ. But, as shown in figure 10(*b*), when $\phi \neq 90^\circ$, there is a small angle between ϕ and ψ_p, a result of (x–z) turbulent flow coupling.

5.2. *Velocity profiles*

Mean-velocity components scaled with u_τ and w_τ are shown in figure 11 for $\phi = 45^\circ$. The plots are in inner scaling relative to the respective top and bottom walls as defined by (3.8*a–d*). Also shown are modified log laws as red dashed and dash-dotted lines calculated with (3.6)–(3.7) using (ψ_b, ψ_t) values obtained from modelling and again assuming $\psi_{q,t} = \psi_t$ and $\psi_{q,b} = \psi_b$. The empirical log lines agree well with the DNS for the pure Couette flows and pure Poiseuille limits. Mean velocities U_b^+ and U_t^+ are shown in figure 11(*a*,*c*). When θ gradually increases from 0° to 90°, the DNS deviates from the log line for Couette flow and then returns to that for Poiseuille flow, which is consistent with the PCP flow DNS of Cheng *et al.* (2023). The z mean-velocity profile W_b^+ is shown in figure 11(*b*), which first increases and then decreases with increasing θ. Figure 11(*d*) shows W_t^+, which gradually increases with increasing θ, and the log law fits well with all cases from $\theta = 15^\circ$ to $\theta = 90^\circ$.

Figure 12 shows the resultant velocity magnitude scaled with q_τ and the velocity gradient indicator function for both walls. The log law is calculated in the same way as for figure 5. Figure 12(*a*,*b*) shows Q_b^+ and Q_t^+. Similar to the results of figure 11, deviation first from and then back to the empirical log law can be observed. The indicator functions Ξ_b and Ξ_t are plotted in figure 12(*c*,*d*). An incipient plateau near $1/0.41$ can be seen in pure Couette flow, while when $\theta = 90^\circ$, the velocity gradient is around $1/0.384$, but the plateau is not well developed owing to the relatively low Reynolds number.

5.3. *Mean-flow velocity vector twist*

Twist behaviour of the resultant mean-velocity vector is a salient feature of GCP flow. The variation of the mean-velocity twist angle as a function of y depends on the chosen frame

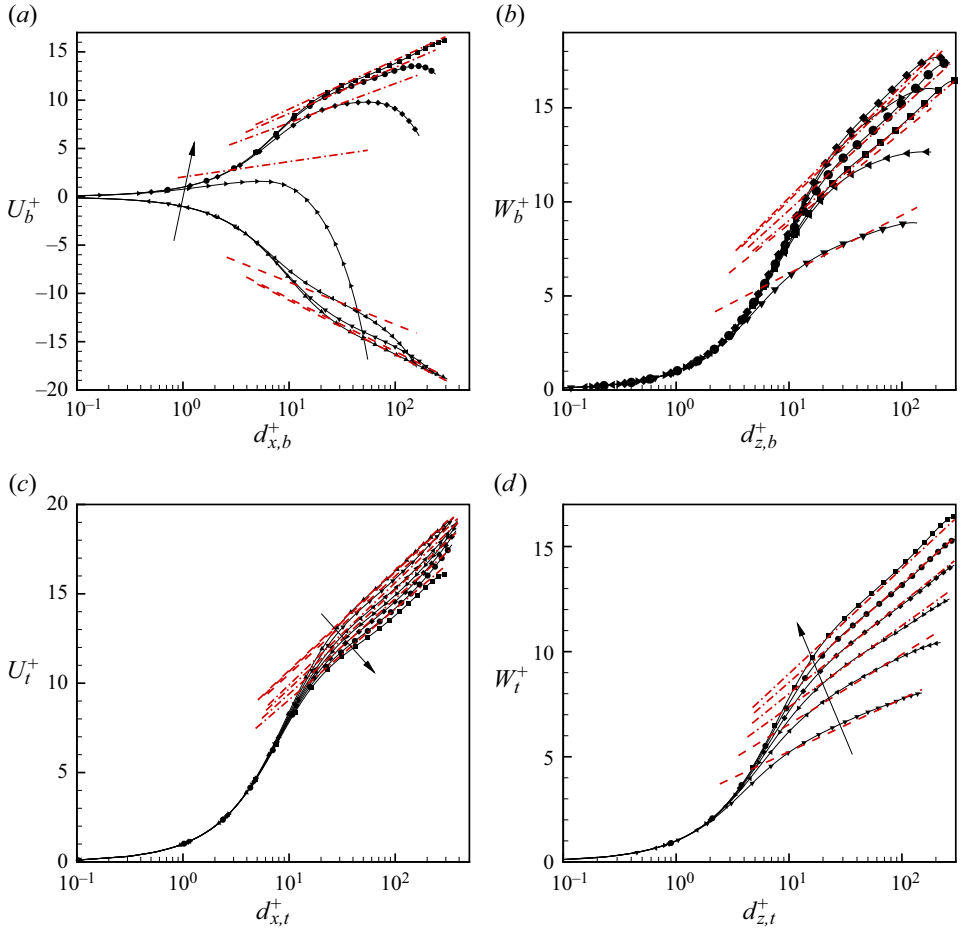

Figure 11. Mean-velocity components for top and bottom walls scaled with u_τ and w_τ, respectively, for $\phi = 45^\circ$. The modified log laws shown as red dash and dash-dotted lines are as calculated from (3.6), (3.7) using ψ_b, ψ_t from the mean-flow modelling. Results are shown for (*a*) U_b^+, (*b*) W_b^+, (*c*) U_t^+, (*d*) W_t^+. Key: ▲: $\theta = 0^\circ$, ▼: $\theta = 15^\circ$, ◀: $\theta = 30$, ▶: $\theta = 45^\circ$, ♦: $\theta = 60^\circ$, ●: $\theta = 75^\circ$, ■: $\theta = 90^\circ$. The black arrows indicate increasing θ.

of reference. For clarity, we denote twist angles by ψ_q for the laboratory reference frame, $\psi_{q,t}$ for the reference frame with the top wall stationary and $\psi_{q,b}$ for the reference frame with the bottom wall stationary. In contrast, the shear-stress angles at each wall (ψ_b, ψ_t) are frame independent. Owing to the boundary conditions at each wall, in the laboratory reference frame the twist angle limits are $\psi_q(y \to -h) \to 0^\circ$ while $\psi_q(y \to h) \to 180^\circ$ for almost all flows with the exception $\theta = 90^\circ$ where $\psi_q(y) = \phi$.

5.3.1. *Laboratory reference frame*

For laminar flow, analysis of ψ_q is straightforward and results are given in Appendix A. For turbulent flow, predictions of $\psi_q(y)$ in the laboratory reference frame can be obtained from the mean-flow modelling of § 4 by direct evaluation of the second equation of (2.5*a–d*), following numerical solution of the model equations for each (ϕ, θ). Figure 13 shows the twist angle displayed as $\psi_q(y)$ for different θ at fixed ϕ. Symbols are DNS values while the dashed lines show model results. Additional model results with $\theta = 1^\circ, 2.5^\circ, 5^\circ$ are also

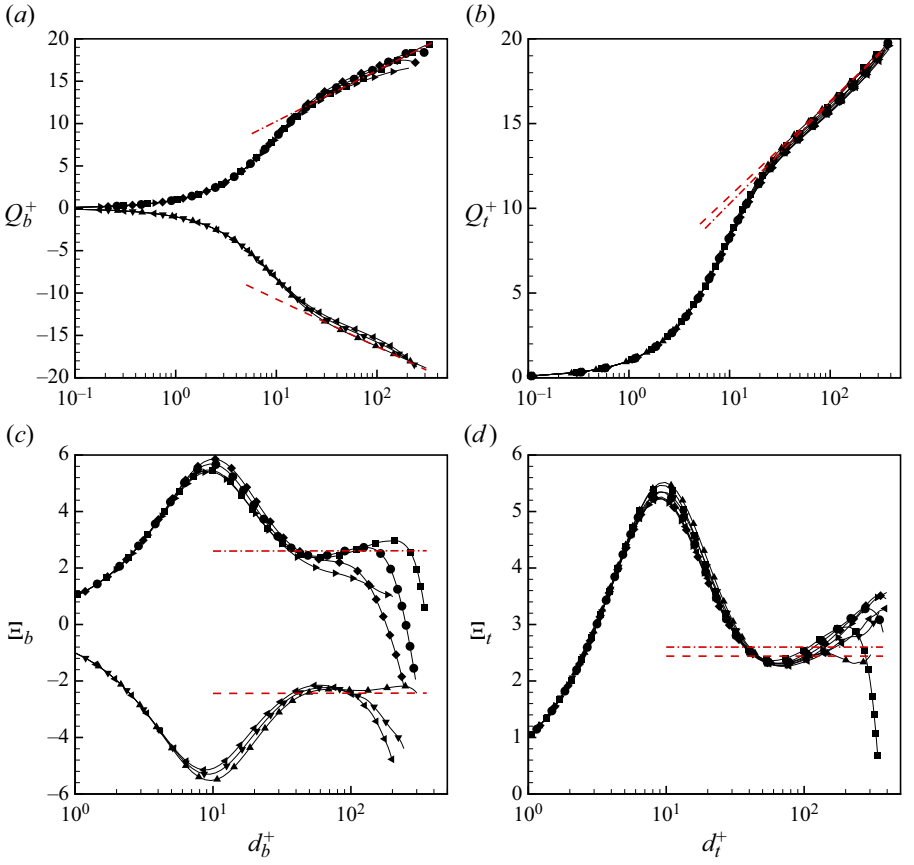

Figure 12. Resultant velocity magnitude scaled with q_τ and velocity gradient indicator function for $\phi = 45°$. The log relation is as for figure 5. Results are shown for (*a*) Q_b^+, (*b*) Q_t^+, (*c*) Ξ_b, (*d*) Ξ_t. See figures 4 or 11 for symbol key.

included outside the range of the DNS. The $\psi_q(y)$ plots show similar qualitative features to their equivalents for laminar flow as shown in figure 22 in Appendix A, but with different profile shapes.

Results for antisymmetric flow in the x direction ($u(-y) = -u(y)$) with $\phi = 90°$ are shown in figure 13(*a*) while figure 13(*b*) shows $\phi = 45°$ where the antisymmetry in $u(y)$ and symmetry in $w(y)$ are broken, In pure PC flow with $\theta = 0°$, then $\psi_q = 0°$ for $-1 \leq y < 0$ and $\psi_q = 180°$ in $0 < y \leq 1$, while for pure PP flows with $\theta = 90°$, $\psi_q = \phi$. On the centreline at $y = 0$, $\psi_q = \phi$ can be observed for all flows. On the top channel half, at fixed $y > 0$, ψ_q reduces rapidly as θ is increased, a trend that is much stronger than for laminar flow at the same ϕ. In the range $15° \leq \theta \leq 75°$, the strong variation in $\psi_q(y)$ at fixed θ is apparent. The modelling predictions fit quite well with DNS results with discrepancies mainly attributable to approximating ψ_q by the top- and bottom-wall shear-stress vectors in the respective reference frames. This is now discussed.

5.3.2. *Reference frame with wall stationary*

Since, for $\phi = 90°$, the wall-moving velocity-difference vector is perpendicular to the volume-flow vector and the mean velocity shows symmetries, we consider only the top

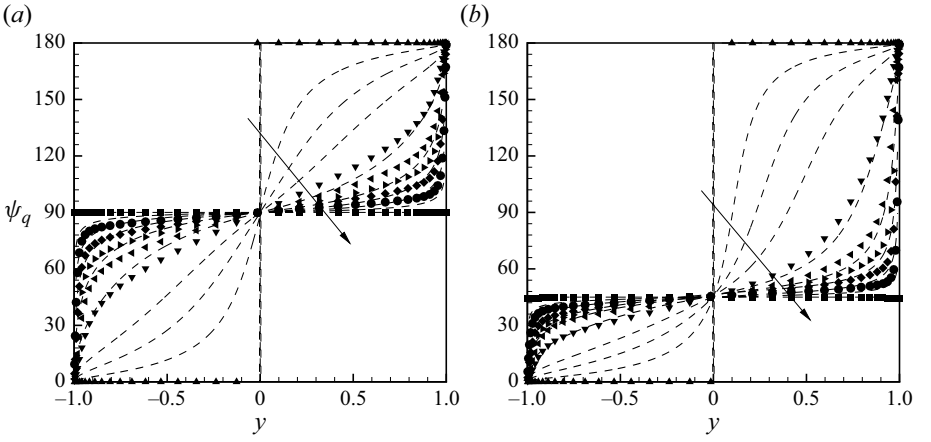

Figure 13. Mean-flow velocity twist angle ψ_q as defined in (2.5*a–d*): (*a*) $\phi = 90°$, (*b*) $\phi = 45°$. Symbols, DNS results; see figures 4 or 11 for symbol key. Dashed lines, modelling results. Also shown are additional modelling results for $\theta = 1°, 2.5°$ and $5°$ (from top to bottom with $y > 0$). The black arrows indicate increasing θ.

half-channel in the reference frame where the top wall is stationary. In this reference frame $\psi_{q,t}(y \to h) \to \psi_t$. In order to visually appreciate the twist behaviour, figure 14 illustrates the resultant mean-velocity vectors in (U, W, y) space for $\phi = 90°$.

In figure 14(*a–g*) three-dimensional velocity vectors $\boldsymbol{Q_t}(y)$ are shown as bundles of red arrows. These are interpolated with a red-coloured surface to show the twist behaviour, while the blue plane is a reference surface parallel to the wall skin-friction coefficient vector at angle ψ_t on the top wall. When θ increases from the PC flow of figure 14(*a*), the surface deviates from the x–y plane and finally approaches the y–z plane at $\theta = 90°$, which is PP flow in the z direction. The reference skin-friction plane and the velocity plane are generally not parallel.

To quantify the twisting behaviour with wall distance, a twist angle deviation $\Delta\psi_{q,t}$ is defined as $|\psi_{q,t}(y) - \psi_t|$, the absolute angle difference between the velocity vector at y and the wall skin vector. In figure 14(*h*) the red dots are the DNS results of $\Delta\psi_{q,t}(y)$ for $\phi = 90°$ and $Re = 6000$, while the blue surface is the reference surface for laminar flow. The general trends of turbulent and laminar flows are similar, where $\Delta\psi_{q,t}$ gradually increases off from the wall. When θ increases from 0°, generally $\Delta\psi_{q,t}$ first increases and then decreases with increasing θ, although the maximum value of $\Delta\psi_{q,t}$ in turbulent flows are much smaller compared with the laminar equivalents.

Figure 15 shows the three-dimensional resultant mean-velocity vector and deviation in the top-wall and bottom-wall reference frames for $\phi = 45°$. As in figure 14, the flow gradually changes from PC flow in the x direction to pure PP flow at an angle of 45°. In figure 15(*a,b*) we plot only the mean-velocity vectors at $\theta = 45°$, which corresponds to the maximum deviation among cases with different θ.

Figure 15(*c,d*) shows the deviation $\Delta\psi_{q,t}$ and $\Delta\psi_{q,b}$ for $\theta = 0° \sim 90°$. In the top-wall reference frame (right), the rotation of mean-flow velocity vectors is substantially smaller and hard to recognize. In the bottom-wall reference frame (left), similarly as in figure 14, the deviation $\Delta\psi_{q,b}$ also first increases and then decreases with increasing θ, while the maximum value is larger than that for $\phi = 90°$ flows.

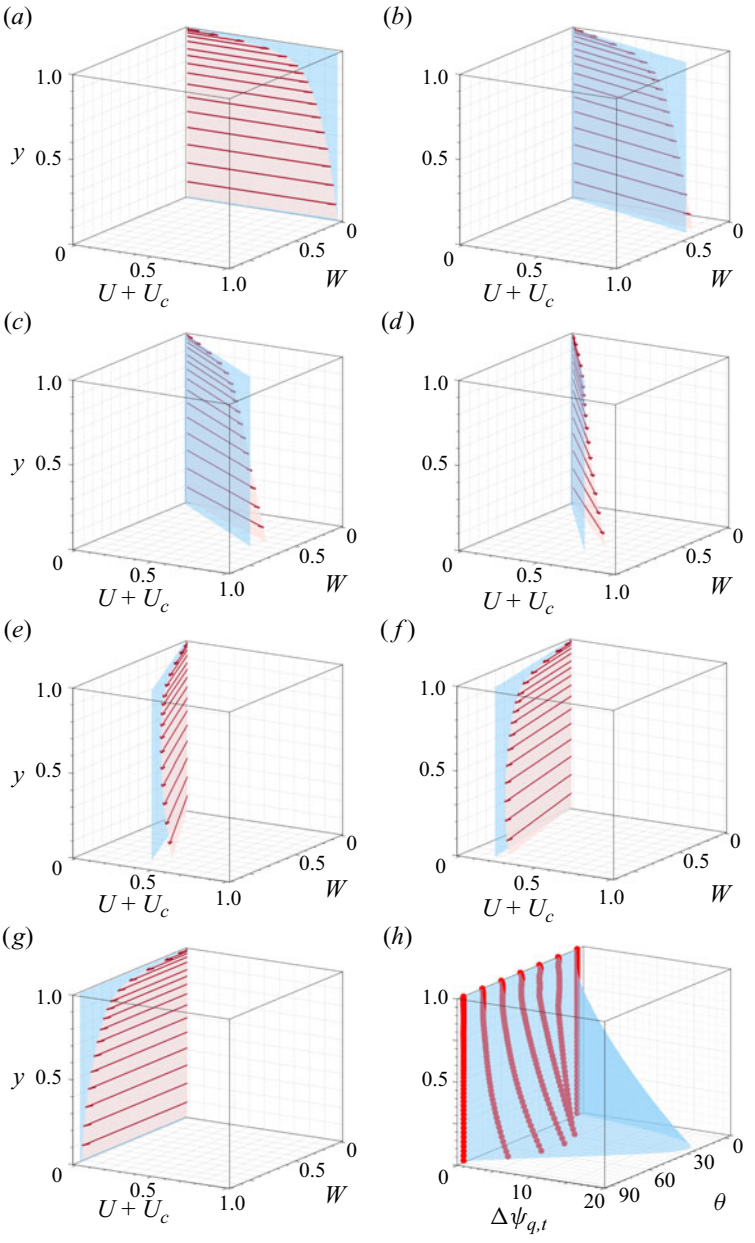

Figure 14. (*a–g*) Mean-velocity vectors in the top-wall reference frame, $(U + U_c, W)$, for $\phi = 90^\circ$ (OCP), with $\theta = 0^\circ$, 15°, 30°, 45°, 60°, 75°, 90°. The red arrows denote DNS results, expanding an interpolating surface coloured red. The vertical blue plane aligns with ψ_t. (*h*) Twisting angle deviation $\Delta\psi_{q,t}(y) = |\psi_{q,t}(y) - \psi_t|$. Red dots are for numerical results and the blue surface for laminar flow.

6. Spectra and flow visualization

6.1. *Premultiplied one- and two-dimensional spectra*

One-dimensional velocity spectra expressed in log-wavenumber coordinates have proven a powerful tool in the diagnostic analysis of canonical wall-bounded turbulent flows,

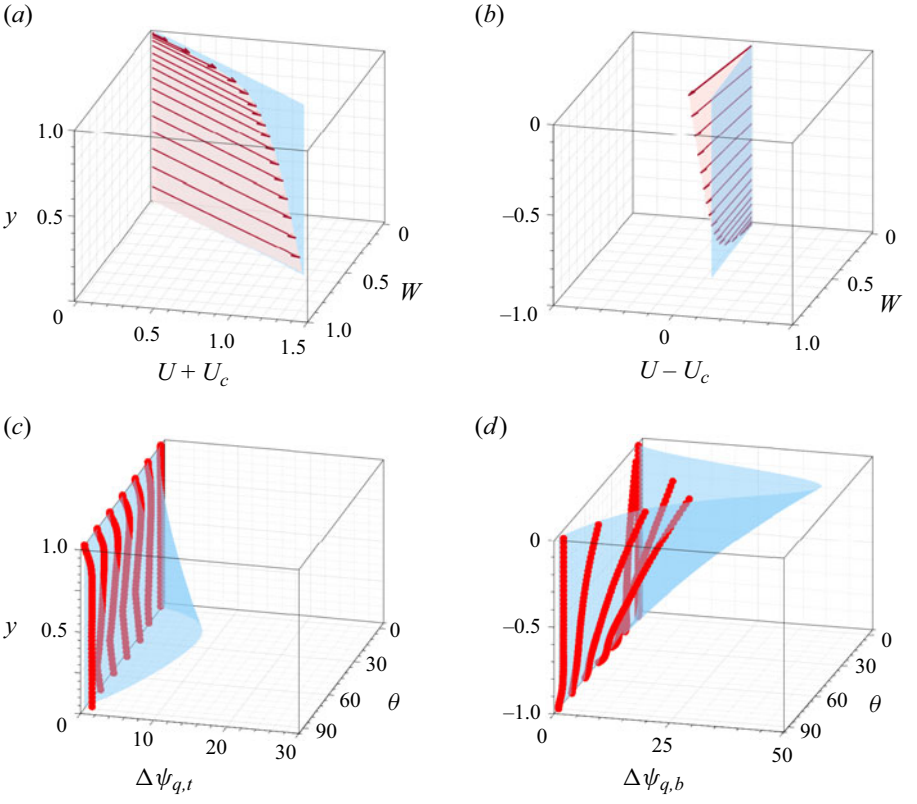

Figure 15. Twist behaviour for GCP flow with $\phi = 45°$. (*a*) Mean-velocity vector $(U + U_c, W)$ in top-wall reference frame, (*b*) $(U - U_c, W)$ in bottom-wall reference frame, (*c*) twist angle deviation $\Delta\psi_{q,t}(y)$ in top-wall reference frame, (*d*) $\Delta\psi_{q,b}(y)$ in bottom-wall reference frame. See figure 14 for symbol key.

suggesting the existence of k^{-1} (Perry, Henbest & Chong 1986; del Álamo *et al.* 2004; Lee & Moser 2015) and $k^{-5/3}$ Kolmogorov-like regimes (see Perry *et al.* 1986). The premultiplied energy spectrum $k\Phi(k)$ has the property that its integral with respect to the log-transformed wavenumber $\log_{10} k$ gives the turbulent kinetic energy. Premultiplied spectra are then useful in analysing the distribution of turbulent energy at different length scales. A striking example is the identification of very-large-scale, longitudinal structures at sufficiently large Re_τ, as observed from their footprint in the wall-normal variation of the k_x premultiplied spectrum of the streamwise velocity $\Phi_{uu}(k_x)$ (Hutchins & Marusic 2007).

Although our $Re = 6000$ is perhaps too low to produce the proposed k^{-1} scaling range, we nonetheless explore premultiplied spectra for OCP flow with $\phi = 90°$ in order to investigate the scale distribution of kinetic energy and its changes with θ for this class of flows. For all cases, the centreline where $d_t^+ = h^+ = Re_\tau$ is on top of each coloured graph boundary. Figure 16 shows the k_x-premultiplied 1-D spectra as a colour-contour plot in $(\log_{10} d_t^+, \log_{10}(k_x h))$ coordinates for different θ. Three columns show spectra of (u, v, w) and the fourth shows the cross-spectrum of u and w computed as the magnitude of $\hat{u}(k)\hat{w}^*(k) + \hat{u}^*(k)\hat{w}(k)$, where the hat denotes the Fourier coefficient and the asterisk is the complex conjugate. The k_x-premultiplied 1-D spectra for PC flow with $\theta = 0°$ and PP flow with $\theta = 90°$ show similar features to the corresponding results of Lozano-Durán

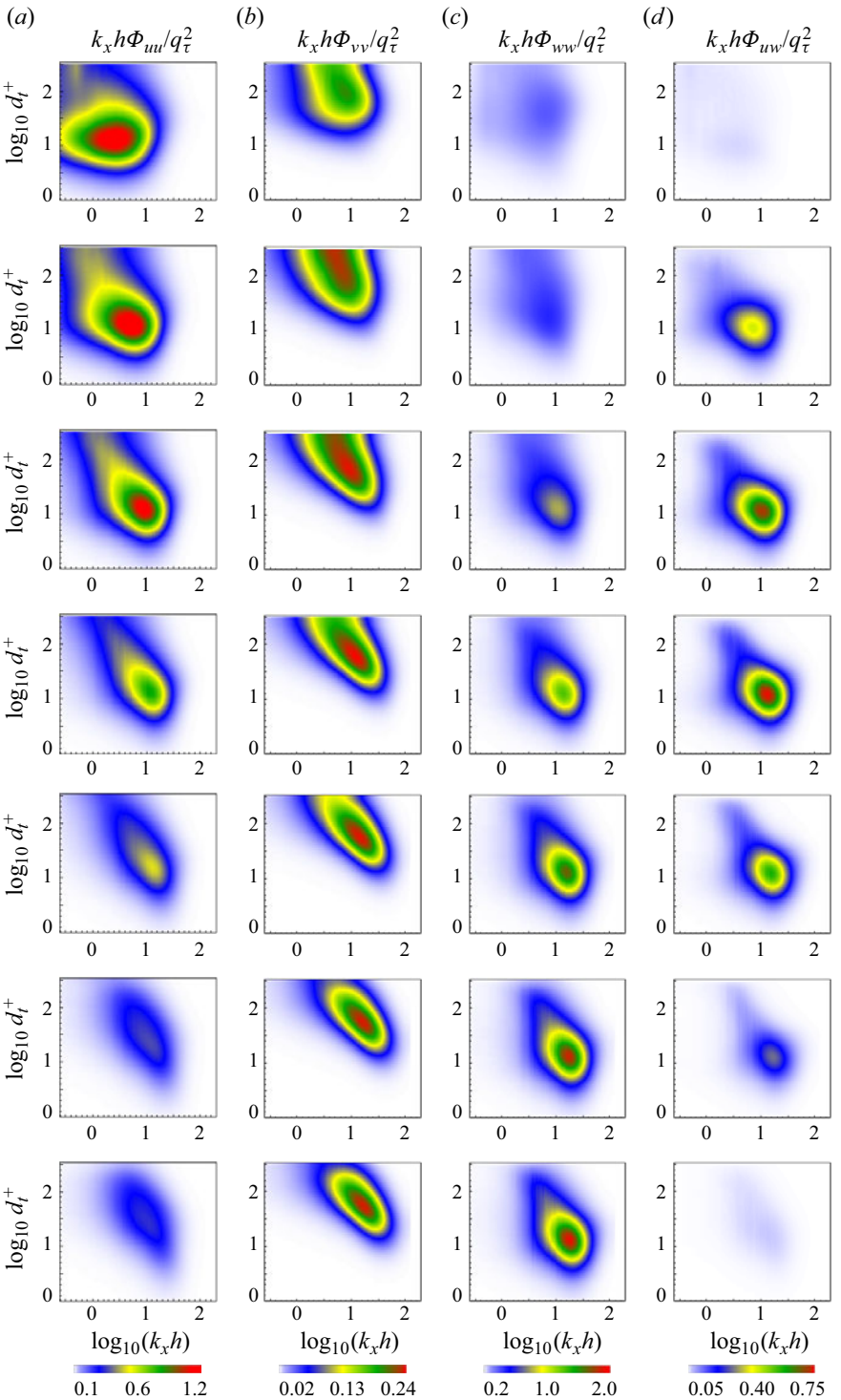

Figure 16. Contours of k_x-premultiplied 1-D spectra for OCP flow ($\phi = 90°$): (*a*) $k_x h\Phi_{uu}/q_\tau^2$, (*b*) $k_x h\Phi_{vv}/q_\tau^2$, (*c*) $k_x h\Phi_{ww}/q_\tau^2$, (*d*) $k_x h\Phi_{uw}/q_\tau^2$. From top to bottom: θ from 0° to $\theta = 90°$ with increments of 15°.

& Jiménez (2014) and Lee & Moser (2018). As θ increases from $0^\circ \rightarrow 90^\circ$ in figure 16, spectra depict the transition from PC flow in the x direction to PP flow in the z direction. The $k_x\Phi_{uu}$ spectrum shows a peak near $y^+ \approx 15$ that moves in the increasing k_x direction as θ increases, signalling the tendency towards smaller length scales as the x axis changes from the effective longitudinal to the transverse direction. In figure 16(*a*,*b*) the width of the spectral humps for both $k_x\Phi_{uu}$ and $k_x\Phi_{vv}$ gradually decrease with increasing θ, indicating that the distribution of energy is more concentrated over a narrower range of scales. The cross-spectrum $k_x\Phi_{uw}$ shows a strong peak at $\theta = 45^\circ$.

The narrow low-wavenumber spike or band in $k_x\Phi_{uu}$ that can be seen near $k_xh \approx 0.5$ for $\theta = 0^\circ$ corresponds to a length scale of about $12.5h$. Direct numerical simulations at $Re_\tau = 500$ by Lee & Moser (2018) show three similar low-wavenumber peaks with the strongest occurring at $k_xh \approx 0.4$. This agreement shows that the present computational domain, although relatively short in the x direction, can nonetheless capture the principal features of streamwise flow structures.

One-dimensional k_z-premultiplied spectra are shown in figure 17. All spectra for pure Couette flow at $\theta = 0^\circ$ show a narrow spike or band centred around small positive $\log_{10}(k_zh)$, which can be interpreted as the spectral signature of coherent streamwise rolls (Tsukahara, Kawamura & Shingai 2006) whose mean spacing is of the order of several channel half-heights in the transverse (for $\theta = 0^\circ$) z direction, independent of the size of the computational domain (Cheng *et al.* 2022). This spike persists slightly at $\theta = 15^\circ$ but is not present at larger θ, indicating the attenuation of roll structures with increasing θ.

Premultiplied spectra $k_z\Phi_{uu}$, $k_z\Phi_{vv}$ and $k_z\Phi_{ww}$ display a low-wavenumber peak. For $k_z\Phi_{uu}$ and $k_z\Phi_{vv}$, in pure PC flow with $\theta = 0^\circ$, two peaks are visible. The greater peak in the narrow spike reaches a maximum value at the centreline, while for $k_x\Phi_{ww}$, it reaches a maximum value at about $d_t^+ = 100$ and decreases to a smaller value at the flow centreline. When θ gradually increases from 0°, the peak in the narrow spike of all four spectra quickly disappears and can no longer be observed, which indicates the disappearance of the large-scale, streamwise oriented roll structures. In addition, it can also be observed that the shape of the energy spectrum changes from the Couette-type flow in the x direction to the Poiseuille-type flow in the z direction. For $k_z\Phi_{uu}$ in figure 17(*a*), as θ increases, the flow in the x direction gradually weakens, so the energy spectrum decreases correspondingly. In figure 17(*b*,*c*) showing $k_z\Phi_{vv}$, $k_z\Phi_{ww}$, as θ increases, the respective peaks near the wall gradually move in the direction of decreasing k_z, that is, towards of larger length scales, which accompanies a structural change in the spectra shape.

In the Φ_{v-v} spectra portraits in both the x and z directions, for Couette-type flow at low θ, the contours extend across the channel centreline, while in Poiseuille-type flow with large θ, closed contours are observed. Similar phenomena have been shown by Lee & Moser (2018). These effects can be attributed to lower–upper half-channel flow symmetry changes and breaking that accompanies θ variations in the range $0^\circ < \theta < 90^\circ$, as the flow transitions from PC to PP flow with corresponding changes to flow structure. For pure PP flow ($\theta = 90^\circ$), the mean-velocity profile is symmetric, resulting in zero turbulent shear stress at the channel centre and corresponding decreased wall-normal turbulent intensities. In contrast, for PC flow ($\theta = 0^\circ$), the mean-x velocity profile is antisymmetric about the flow centre plane. As a result, as shown in corresponding plots by Pirozzoli *et al.* (2014) in their DNS up to $Re_\tau = 986$, the turbulent shear stress is finite at the centreline and the wall-normal turbulent intensity generally shows a plateau. For $\phi = 90^\circ$, for all θ, the x-mean-velocity profile is antisymmetric while the mean z profile is symmetric. For all other (θ, ϕ), component mean-velocity profiles display no symmetry/anti-symmetry properties.

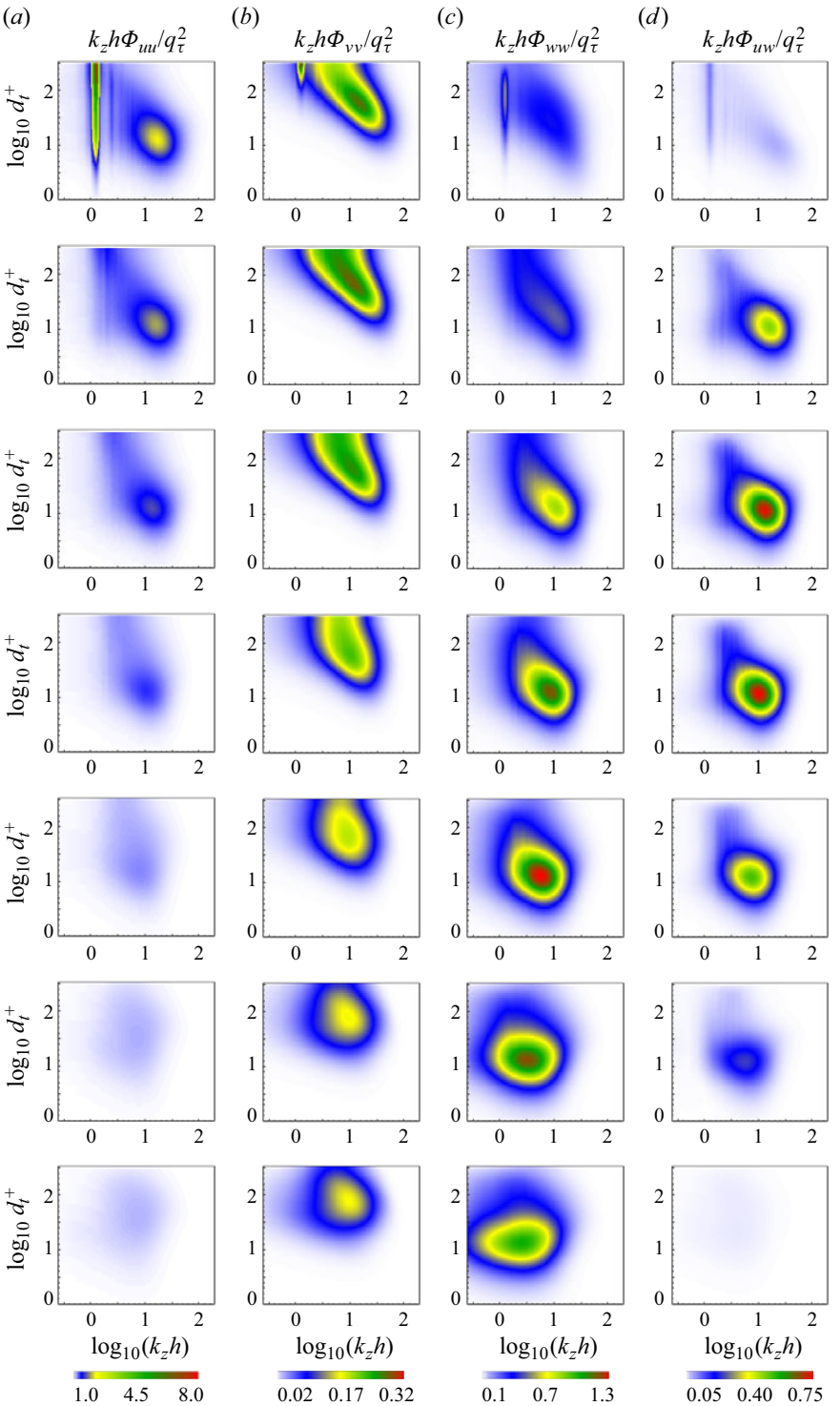

Figure 17. Contours of k_z-premultiplied 1-D spectra for OCP flows ($\phi = 90^\circ$): (*a*) $k_z h\Phi_{uu}/q_\tau^2$, (*b*) $k_z h\Phi_{vv}/q_\tau^2$, (*c*) $k_z h\Phi_{ww}/q_\tau^2$, (*d*) $k_z h\Phi_{uw}/q_\tau^2$. From top to bottom: $\theta = 0^\circ$–90° with increments of 15°.

The k_x- and k_z-premultiplied two-dimensional (2-D) spectra at approximately $d_t^+ = 30$ are shown in figure 18. The peaks of both $k_x k_z \Phi_{uu}$ and $k_x k_z \Phi_{vv}$ reach respective maxima with respect to θ variation at $\theta \approx 30^\circ$, $k_x k_z \Phi_{uw}$ achieves a maximum value at $\theta = 45^\circ$, while $k_x k_z \Phi_{ww}$ maximizes at $\theta = 60^\circ$. With an increase in θ, rotation of spectra footprints in the $(\log_{10}(k_x h) - \log_{10}(k_z h))$ plane can be clearly observed. For example, as θ increases, the elongated $k_x k_z \Phi_{vv}$ hump rotates from near alignment with the $\log_{10}(k_z h)$ axis towards alignment with the $\log_{10}(k_z h)$. At $\theta = 45^\circ$, the spectrum shape is almost symmetric about $\log_{10}(k_z h) = \log_{10}(k_x h)$. This demonstrates the reorientation of energetic structures during the transition from Couette to orthogonal Poiseuille flow.

Centreline ($y = 0$) k_x- and k_z-premultiplied, 2-D spectra are shown in figure 19. The peaks of both $k_x k_z \Phi_{uu}$ and $k_x k_z \Phi_{vv}$ reach a maxima at $\theta = 15^\circ$, while both $k_x k_z \Phi_{uw}$ and $k_x k_z \Phi_{ww}$ reach a maxima at $\theta = 30^\circ$. The low-wavenumber peak of $k_x k_z \Phi_{uu}$ can be clearly observed in figure 19(*a*,*d*), which is consistent with the result in figure 17. Compared with figure 18, the rotation of overall premultiplied spectra can still be observed, but the rotation angle is smaller.

6.2. *Large-scale features in GCP flows*

To observe the large-scale flows more clearly, visualization of time-averaged Q fields coloured by vertical velocity v are shown in figure 20 for OCP flows with $\phi = 90^\circ$. Here,

$$Q = -\frac{1}{2}\left[\left(\frac{\partial u}{\partial x}\right)^2 + \left(\frac{\partial v}{\partial y}\right)^2 + \left(\frac{\partial w}{\partial z}\right)^2\right] - \frac{\partial u}{\partial y}\frac{\partial v}{\partial x} - \frac{\partial v}{\partial z}\frac{\partial w}{\partial y} - \frac{\partial w}{\partial x}\frac{\partial u}{\partial z}, \tag{6.1}$$

which is commonly used for vortex identification. The images are a time average of the instantaneous flow field. Four flows are illustrated, each viewed from above the top plate with $\theta = 0^\circ,\ 15^\circ, 30^\circ,\ 45^\circ$. Each figure displays the whole computational domain with the same scale in the three coordinate directions. Isosurfaces with $Q = 0.01$ are plotted and coloured by the wall-normal velocity over ranges tailored for each specific flow.

In figure 20(*a*) with $\theta = 0^\circ$, which is pure Couette flow in the x direction, large-scale roll structures, each of which extends to both walls, meander along the x direction. In the 8π domain in the z direction, five roll pairs are captured, which is consistent with the DNS of Pirozzoli *et al.* (2014). Since the view is from above the upper wall, which is moving in the negative x direction, then the mean-flow velocity angle for $y > 0$ is $\psi_q = 180^\circ$. When θ increases to $\theta = 15^\circ$ in figure 20(*b*), the rolls are obliterated and very-large-scale structures are not visible. Figure 13 shows a very rapid change (decrease) in ψ_q from 180° at a $y > 0$ level in the upper half-channel (where structures are most visible in the view shown), when θ increases in the range 0°–45°. This can be seen in figure 20(*b*) where visible isosurfaces in $y > 0$ are oriented at $\psi_q \approx 135^\circ$–140°, which is largely towards the viewpoint.

Further increase of θ implies increased volume flow in the z direction. In figure 20(*c*), ψ_q in the upper half-channel has rotated further towards the z axis, which continues at $\theta = 45^\circ$ in figure 20(*d*). Here, owing to enhanced transparency within the view, an averaged orientation difference between Q isosurfaces in the upper and lower half-channel subdomains can be perceived. Still further increases in θ show Q-isosurface fields (not shown) that, from the chosen viewpoint, resemble those obtained for pure PP flow.

Visualizations of GCP flows with $\phi \neq 90^\circ$ and varying θ show similar structural changes to those seen in figure 20 but with differing fine details. Their novel, salient features not seen in parallel wall-bounded flows is the wall-normal rotation in

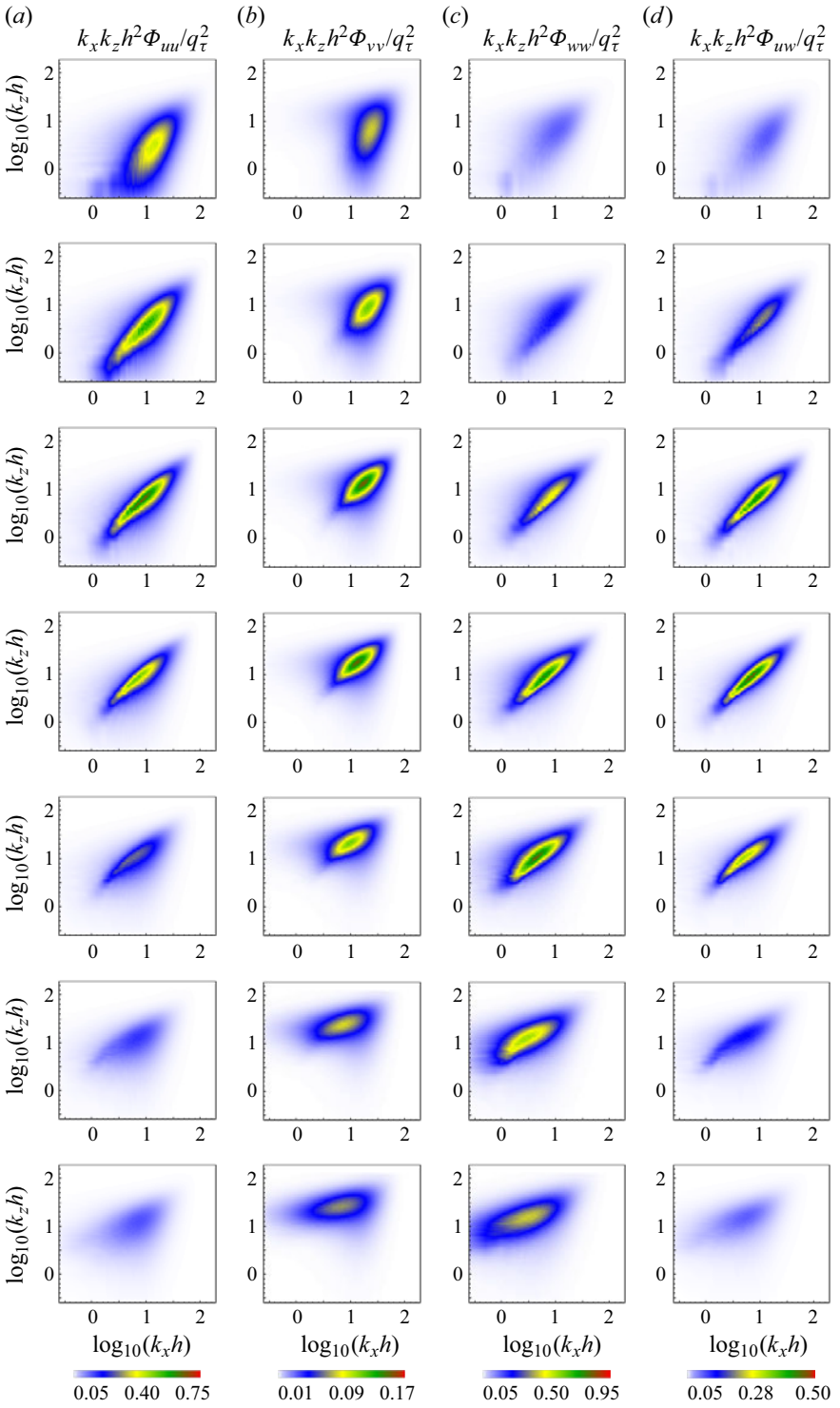

Figure 18. Contours of k_x- and k_z-premultiplied two-dimensional (2-D) spectra at around $d_t^+ = 30$: (*a*) $k_x k_z h^2 \Phi_{uu}/q_\tau^2$, (*b*) $k_x k_z h^2 \Phi_{vv}/q_\tau^2$, (*c*) $k_x k_z h^2 \Phi_{ww}/q_\tau^2$, (*d*) $k_x k_z h^2 \Phi_{uw}/q_\tau^2$. From top to bottom: θ from 0° to $\theta = 90°$ with increments of 15°.

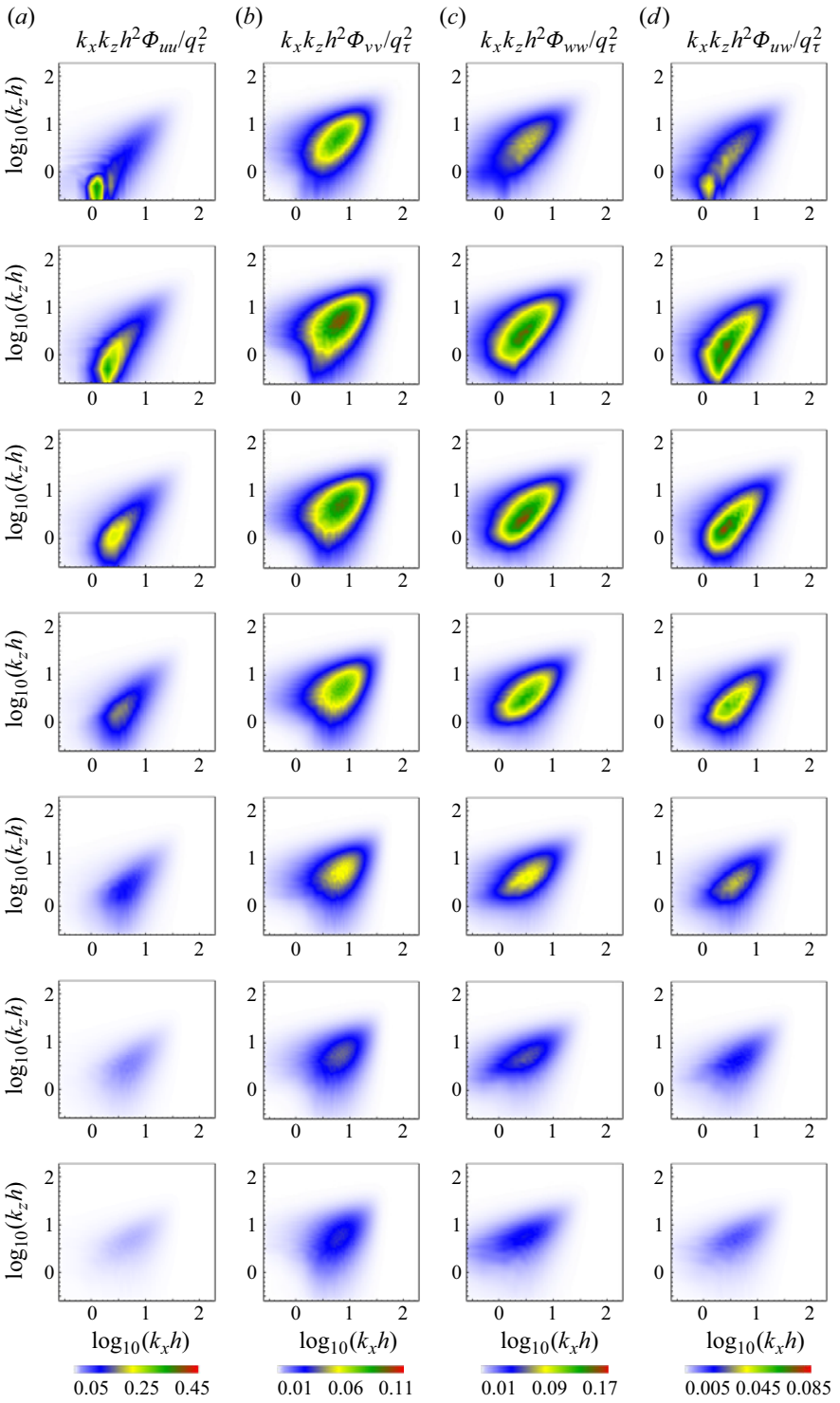

Figure 19. Contours of the k_x- and k_z-premultiplied 2-D spectra on the centre line $y = 0$: (*a*) $k_x k_z h^2 \Phi_{uu}/q_\tau^2$, (*b*) $k_x k_z h^2 \Phi_{vv}/q_\tau^2$, (*c*) $k_x k_z h^2 \Phi_{ww}/q_\tau^2$, (*d*) $k_x k_z h^2 \Phi_{uw}/q_\tau^2$. From top to bottom: θ from 0° to $\theta = 90^\circ$ with increments of 15°.

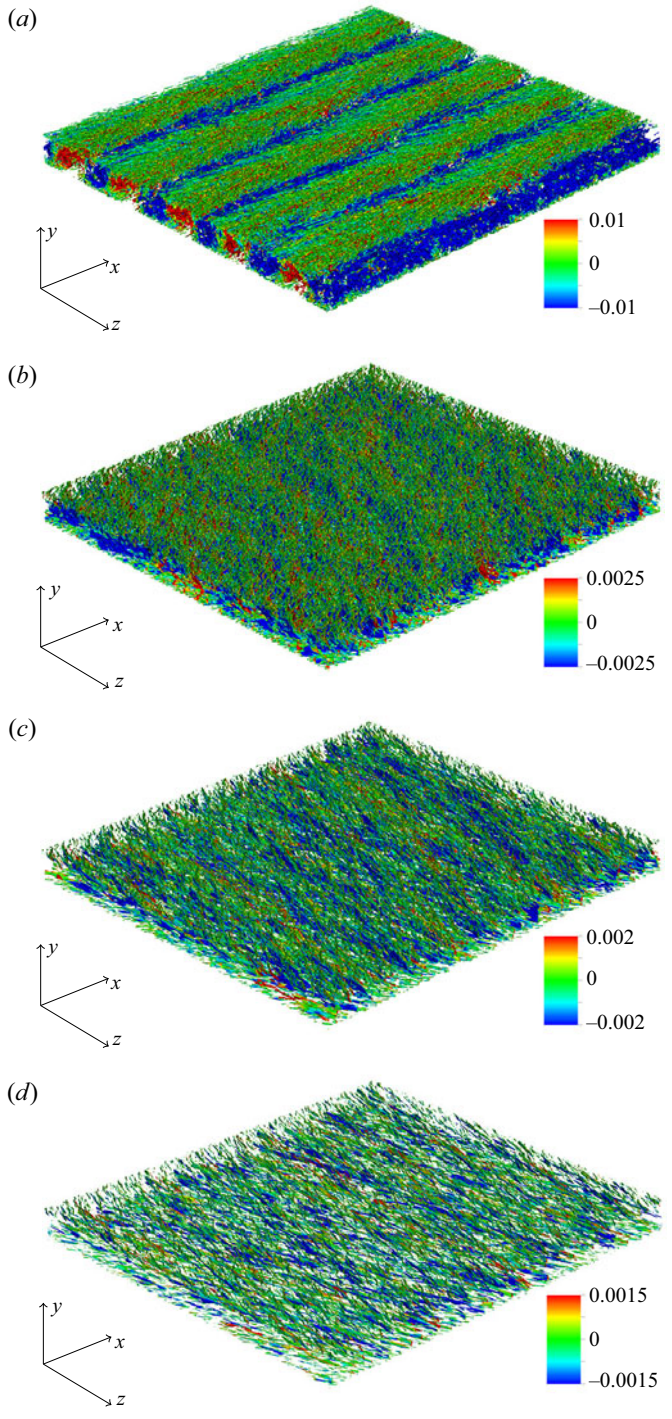

Figure 20. Visualization of time-averaged Q fields coloured by vertical velocity v for OCP flow with $\phi = 90°$. Here $Q = 0.01$ for all cases. Results are shown for (*a*) $\theta = 0°$, (*b*) $\theta = 15°$, (*c*) $\theta = 30°$, (*d*) $\theta = 45°$.

structure orientation. A detailed study of the physics underlying cross-flow interactions in the presence of wall-normal, mean-velocity twist would seem of interest to understanding the physics of three-dimensional, wall-bounded turbulent flows. This would require new diagnostic and interpretive techniques, which is beyond the scope of the present investigation.

7. Conclusion

We have described DNS and modelling of GCP flow, which can be characterized by a global Reynolds number Re and two angles (θ, ϕ) that characterize respectively the weighting of Poiseuille to Couette flow ($\tan\theta$) and the inclination of the volume flow to the plate relative-velocity vectors. Simulations have fixed $Re = 6000$ with θ and ϕ evenly distributed in $[0, 90^\circ]$ with increments of 15°.

Orthogonal Couette–Poiseuille flow corresponds to $\phi = 90^\circ$ where the volume flow is normal to the plate velocity-difference vector for all θ. For these flows, the mean velocity satisfies symmetry $(U(-y), W(-y)) = (-U(y), W(y))$, so that it is sufficient to focus on either half-channel. With inner scaling using the full skin-friction velocity, the magnitude of the mean velocity displays a log-like region with, for $Re = 6000$, a Kármán parameter that may be different for Couette- and Poiseuille-type flows. The (x, z) component mean velocities show modified log-like regions in inner scaling based on component friction velocities and with parameters that are well predicted by a coordinate mapping from the fitted mean-flow log relation.

Mean-flow modelling in several channel regions is developed based on the use of empirical log and log-wake relations together with the approximation that the local mean-velocity twist angle in each subregion is aligned with the orientation of the skin-friction vector at the wall, in the wall reference frame. This is considered a high Re approach. The model provides predictions of four skin-friction coefficients comprising (x, z) components of the skin-friction vector at each wall as functions of (Re, θ, ϕ) and also mean-velocity profiles from which wall-normal, velocity twist distributions can be obtained. These all show general agreement with DNS results at $Re = 6000$ with differences attributable both to the relatively low present Re and also to possible flow relaminarization in a small region of (θ, ϕ) space that is not included in the model. In the top-wall reference frame, the velocity twist angle distributions show deviations from a plane defined by the corresponding shear-stress vector at the wall. Predictions of the offset between the pressure-gradient and bulk volume-flow vectors also show broad agreement with the DNS.

Owing to the three-dimensional character of the mean-flow velocity field, turbulent-intensity profiles have proved difficult to characterize. Premultiplied 1-D and 2-D spectra can be constructed and show interesting features and changes in the scale distribution of turbulent kinetic energy during the transition from Couette-type to Poiseuille-type flow. At $\phi = 90^\circ$ with mean-velocity symmetries, as θ increases from 0° to 90°, the peak in the k_x premultiplied spectrum gradually moves towards the direction of increasing k_x, that is, towards smaller scales. Rotation of the energy spectrum in the $(y^+ - \log_{10}(k_x h)$ plane is observed. For the k_z-premultiplied spectra, when $\theta = 0^\circ$ for pure Couette flow, there exists low-wavenumber spikes in all spectra, indicating the presence of large-scale, streamwise rolls with approximate spatial periodicity in the z direction. At $\theta = 15^\circ$, the spike has disappeared. As θ increases from 15° to 90°, the spectral peak gradually moves in the direction of decreasing k_z, that is, towards larger scales. Similarly, owing to faster velocity near the moving wall in the laboratory frame, rotation of the spectral-hump footprint is observed.

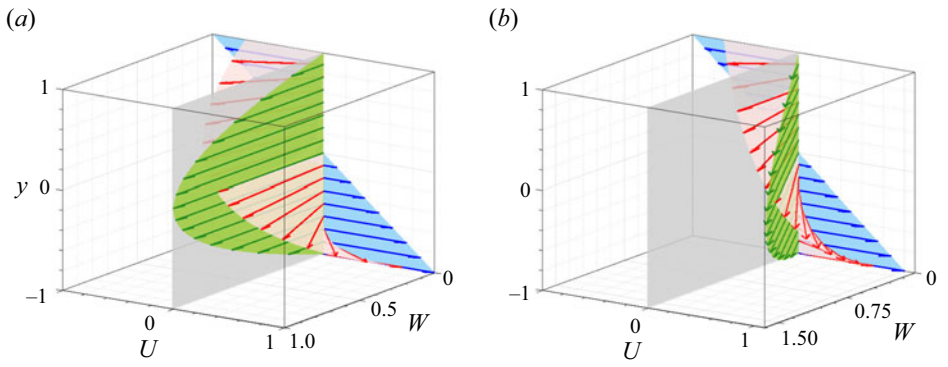

Figure 21. Three-dimensional velocity vectors for laminar flow: (*a*) $\phi = 90°$, (*b*) $\phi = 45°$. Blue: $\theta = 0°$, red: $\theta = 45°$, green: $\theta = 90°$. The grey is the reference surface parallel to the y–w plane.

Funding. This work was supported by the National Natural Science Foundation of China (nos 12172352, 12388101), the Strategic Priority Research Program of the Chinese Academy of Sciences (no. XDB0500300) and the National Key R&D Program of China (no. 2022YFA1005200). Part of the simulations were carried out in the Cray XC40, Shaheen, at KAUST.

Declaration of interests. The authors report no conflict of interest.

Author ORCIDs.
D.I. Pullin https://orcid.org/0009-0007-5991-2863;
W. Cheng https://orcid.org/0000-0003-3960-4162;
X. Luo https://orcid.org/0000-0002-4303-8290.

Appendix A. Laminar GCP flow

Laminar GCP flow is a linear combination of PC flow in the x direction and PP flow in the ϕ direction. Its solution can be written as

$$\left.\begin{aligned} u(y)/U_0 &= -Y\cos\theta + \tfrac{3}{2}(1-Y^2)\sin\theta\cos\phi, \\ w(y)/U_0 &= \tfrac{3}{2}(1-Y^2)\sin\theta\sin\phi, \end{aligned}\right\} \tag{A1}$$

with $Y = y/h$. The three velocity components are

$$U_c = U_0\cos\theta, \quad U_{Vx} = U_0\sin\theta\cos\phi, \quad U_{Vz} = U_0\sin\theta\sin\phi. \tag{A2a–c}$$

Laminar-flow skin-friction coefficients can then be obtained as

$$\left.\begin{aligned} C_{ft,x} = (6\sin\theta\cos\phi + 2\cos\theta)/Re,\ C_{fb,x} = (6\sin\theta\cos\phi - 2\cos\theta)/Re, \\ C_{ft,z} = C_{fb,z} = 6\sin\theta\sin\phi/Re. \end{aligned}\right\} \tag{A3}$$

The streamwise component $C_{fb,x} = 0$ corresponds to $\theta_c = \arctan[(3\cos\phi)^{-1}]$.

Visualizations of the three-dimensional velocity vector variation across the channel are shown in figure 21(*a*) for $\phi = 90°$ and in figure 21(*b*) for $\phi = 45°$. Each plot shows the magnitude and twist angle variation with the wall-normal coordinate y for three values of $\theta = 0°$, $45°$ and $90°$. When $\theta = 0°$, $u(y)$ is the linear-Couette profile in the x direction with $w = 0$. When $\theta = 90°$, $u(y)$ and $w(y)$ combine into a pure Poiseuille profile in the ϕ direction. For $\theta = 45°$, the mean flow is twisted along the y direction.

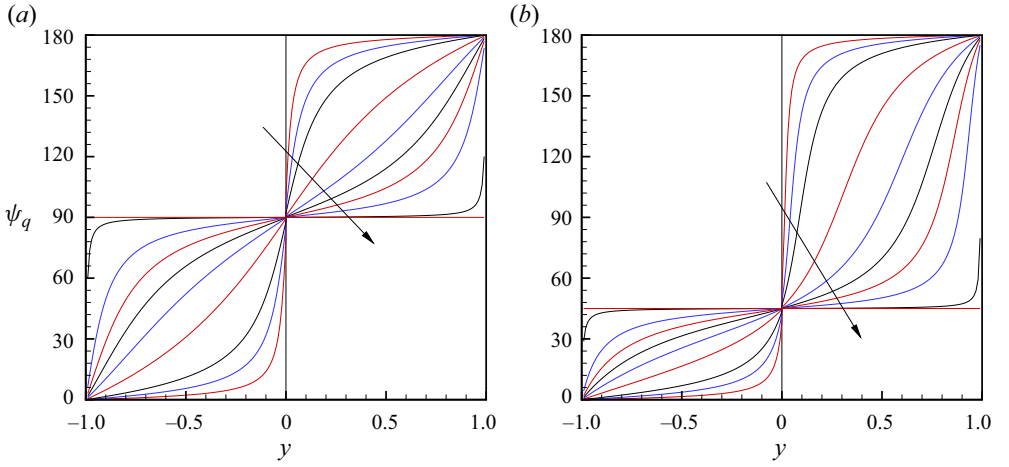

Figure 22. Mean-flow velocity twist ψ_q as defined in (2.5*a–d*) for laminar flows: (*a*) $\phi = 90°$, (*b*) $\phi = 45°$. The black, red and blue lines represent, from top to bottom, $\theta = 0°$, $1°$, $2.5°$, $5°$, $15°$, $30°$, $45°$, $60°$, $75°$, $89°$, $90°$, respectively. The black arrows indicate increasing θ.

Figure 22 shows mean-flow velocity twist angle ψ_q in the laboratory frame of reference as defined in (2.9*a*,*b*) for laminar flows with $\phi = 90°$ and $\phi = 45°$. For each flow, ψ_q varies from $0°$ to $180°$ from the bottom to the top wall. On the centreline $\psi_q = \phi$ for all cases. The position of an inflection point in $\psi_q(Y)$ generally depends on both ϕ and θ. For $\phi = 90°$, this reduces to $9\cot^2\theta = 4(Y^2 + 3)(1 - Y^2)$, implying a corresponding $\theta \approx 21.1°$ for the inflection point to be located at $Y = 0$, which agrees with figure 22(*a*). Between $\theta = 15°$ and $\theta = 30°$ the change from a convex to concave curve shape can be seen.

References

DEL ÁLAMO, J.C. & JIMÉNEZ, J. 2003 Spectra of the very large anisotropic scales in turbulent channels. *Phys. Fluids* **15** (6), L41–L44.

DEL ÁLAMO, J.C., JIMÉNEZ, J., ZANDONADE, P. & MOSER, R.D. 2004 Scaling of the energy spectra of turbulent channels. *J. Fluid Mech.* **500**, 135–144.

BERNARDINI, M., PIROZZOLI, S. & ORLANDI, P. 2014 Velocity statistics in turbulent channel flow up to $Re_\tau = 4000$. *J. Fluid Mech.* **742**, 171–191.

CHENG, W., PULLIN, D.I. & SAMTANEY, R. 2022 Wall-resolved and wall-modelled large-eddy simulation of plane Couette flow. *J. Fluid Mech.* **934**, A19.

CHENG, W., PULLIN, D.I., SAMTANEY, R. & LUO, X. 2023 Numerical simulation of turbulent, plane parallel Couette-Poiseuille flow. *J. Fluid Mech.* **955**, A4.

CHOI, Y.K., LEE, J.H. & HWANG, J. 2021 Direct numerical simulation of a turbulent plane Couette-Poiseuille flow with zero-mean shear. *Intl J. Heat Fluid Flow* **90**, 108836.

COLEMAN, G.N., PIROZZOLI, S., QUADRIO, M. & SPALART, P.R. 2017 Direct numerical simulation and theory of a wall-bounded flow with zero skin friction. *Flow Turbul. Combust.* **99**, 553–564.

GANDÍA-BARBERÁ, S., HOYAS, S., OBERLACK, M. & KRAHEBERGER, S. 2018 Letter: the link between the Reynolds shear stress and the large structures of turbulent Couette-Poiseuille flow. *Phys. Fluids* **30** (4), 041702.

HOYAS, S. & JIMÉNEZ, J. 2006 Scaling of the velocity fluctuations in turbulent channels up to $Re_\tau = 2003$. *Phys. Fluids* **18** (1), 011702.

HUTCHINS, N. & MARUSIC, I. 2007 Evidence of very long meandering features in the logarithmic region of turbulent boundary layers. *J. Fluid Mech.* **579**, 1–28.

JODAI, Y. & ELSINGA, G.E. 2016 Experimental observation of hairpin auto-generation events in a turbulent boundary layer. *J. Fluid Mech.* **795**, 611–633.

JONES, M.B., MARUSIC, I. & PERRY, A.E. 2001 Evolution and structure of sink-flow turbulent boundary layers. *J. Fluid Mech.* **428**, 1–27.

VON KÁRMÁN, T. 1930 Mechanische ahnlichten und turbulenz. In *Proc. Third Intern. Congr. Appl. Mech.*, vol. 1, pp. 85–93.

KIM, J., MOIN, P. & MOSER, R. 1987 Turbulence statistics in fully developed channel flow at low Reynolds number. *J. Fluid Mech.* **177**, 133–166.

KITOH, O., NAKABYASHI, K. & NISHIMURA, F. 2005 Experimental study on mean velocity and turbulence characteristics of plane Couette flow: low-Reynolds-number effects and large longitudinal vortical structure. *J. Fluid Mech.* **539**, 199–227.

LEE, J.H., SUNG, H.J. & ADRIAN, R.J. 2019 Space–time formation of very-large-scale motions in turbulent pipe flow. *J. Fluid Mech.* **881**, 1010–1047.

LEE, M. & MOSER, R.D. 2015 Direct numerical simulation of turbulent channel flow up to $Re_\tau \approx 5200$. *J. Fluid Mech.* **774**, 395–415.

LEE, M. & MOSER, R.D. 2018 Extreme-scale motions in turbulent plane Couette flows. *J. Fluid Mech.* **842**, 128–145.

LOZANO-DURÁN, A. & JIMÉNEZ, J. 2014 Effect of the computational domain on direct simulations of turbulent channels up to $Re_\tau = 4200$. *Phys. Fluids* **26** (1), 011702.

LUCHINI, P. 2018 Structure and interpolation of the turbulent velocity profile in parallel flow. *Eur. J. Mech.* B/*Fluids* **71**, 15–34.

MILLIKAN, C.B. 1938 A critical discussion of turbulent flows in channels and circular tubes. In *Proc. Fifth Intern. Congr. Appl. Mech.*, pp. 386–392.

MOSER, R.D., KIM, J. & MANSOUR, N.N. 1999 Direct numerical simulation of turbulent channel flow up to $Re_\tau = 590$. *Phys. Fluids* **11** (4), 943–945.

NAGIB, H.M. & CHAUHAN, K.A. 2008 Variations of von Kármán coefficient in canonical flows. *Phys. Fluids* **20** (10), 101518.

NAKABAYASHI, K., KITOH, O. & KATOH, Y. 2004 Similarity laws of velocity profiles and turbulence characteristics of Couette-Poiseuille turbulent flows. *J. Fluid Mech.* **507**, 43–69.

ORLANDI, P., BERNARDINI, M. & PIROZZOLI, S. 2015 Poiseuille and Couette flows in the transitional and fully turbulent regime. *J. Fluid Mech.* **770**, 424–441.

OSTILLA-MÓNICO, R., VERZICCO, R., GROSSMANN, S. & LOHSE, D. 2016 The near-wall region of highly turbulent Taylor–Couette flow. *J. Fluid Mech.* **788**, 95–117.

PERRY, A.E., HENBEST, S. & CHONG, M.S. 1986 A theoretical and experimental study of wall turbulence. *J. Fluid Mech.* **165**, 163–199.

PIROZZOLI, S., BERNARDINI, M. & ORLANDI, P. 2011 Large-scale motions and inner/outer layer interactions in turbulent Couette-Poiseuille flows. *J. Fluid Mech.* **680**, 534–563.

PIROZZOLI, S., BERNARDINI, M. & ORLANDI, P. 2014 Turbulence statistics in Couette flow at high Reynolds number. *J. Fluid Mech.* **758**, 327–343.

TELBANY, M.M.M.E. & REYNOLDS, A.J. 1980 Velocity distributions in plane turbulent channel flows. *J. Fluid Mech.* **100** (1), 1–29.

THURLOW, E.M. & KLEWICKI, J.C. 2000 Experimental study of turbulent Poiseuille–Couette flow. *Phys. Fluids* **12** (4), 865–875.

TILLMARK, N. & ALFREDSSON, P.H. 1998 Large scale structures in turbulent plane Couette flow. In *Advances in Turbulence VII*, pp. 59–62. Springer.

TSUKAHARA, T., KAWAMURA, H. & SHINGAI, K. 2006 DNS of turbulent Couette flow with emphasis on the large-scale structure in the core region. *J. Turbul.* **7**, N19.

WEI, T., FIFE, P. & KLEWICKI, J. 2007 On scaling the mean momentum balance and its solutions in turbulent Couette-Poiseuille flow. *J. Fluid Mech.* **573**, 371–C398.

YANG, K., ZHAO, L. & ANDERSSON, H.I. 2017 Turbulent Couette-Poiseuille flow with zero wall shear. *Intl J. Heat Fluid Flow* **63**, 14–27.